

Abstract

The Canary and Madeira Islands are two distinct hotspots in the Central-East Atlantic that are close to each other. Their volcanism is generally attributed to underlying mantle plumes, but the detailed structure of these plumes is still not well understood. The thermal and compositional structure of the plume introduces complexities in the phase transitions of the mantle, which impact the depth and magnitude of seismic discontinuities. We use 1268 high-quality receiver functions from stations located at the two hotspots to detect P-to-s converted phases through a common-conversion point stacking approach and conduct a detailed analysis of mantle seismic discontinuities. The results show that both hotspots are characterized by a thin mantle transition zone (MTZ), with sharp 410 and 660 discontinuities at depths of 429-420 km and 647-664 km, beneath the Canaries and Madeira respectively. The results indicate that the Canary plume crosses the MTZ, whereas the Madeira plume mainly influences the upper portion of the MTZ. Furthermore, we find reliable detections of a sharp X discontinuity beneath the Canaries at 289 km. Its presence suggests the accumulation of silica-rich recycled eclogite at these depths. We also use the amplitudes of P410s and PXs to derive velocity jumps at corresponding discontinuities. Based on these measurements, we estimate that the basalt proportion is 60-80%, with accumulation being more significant in the Canaries than in Madeira. The MTZ thickness, the presence of the X discontinuity, and the high basalt proportion provide compelling evidence for a deep-rooted thermochemical plume beneath the study area.

Plain Language Summary

We examine the Canary and Madeira Islands, two separate groups of islands in the Atlantic Ocean, close to each other. While it is generally accepted that volcanic activity in these regions is driven by underlying mantle plumes, the precise characteristics of these plumes remain relatively unknown. Tomography studies have revealed distinct structures of the plumes, with the Canary plume extending vertically throughout the upper mantle, while the Madeira plume is visible up to a depth of 300 km, beyond which the resolution of the images deteriorates. We use receiver functions, derived from the analysis of seismic waveforms, particularly the conversion of compressional waves to shear waves at seismic discontinuities within the Earth. Receiver functions offer a higher resolution compared to tomographic images, primarily due to their ability to directly measure seismic wave conversions at specific depths, reflecting where mantle minerals change their crystal structure. This analysis provides insights into the variations in temperature and mineral chemistry in the mantle, as both factors influence the depths of crystal rearrangements. Our research provides evidence supporting the existence of a deep-seated thermochemical plume beneath the study area. However, beneath Madeira, the plume may be less vigorous or presently disconnected from its deep source.

1 Introduction

The Canary and Madeira archipelagos are part of two intraplate volcanic provinces in the Central-East Atlantic Ocean close to the African coast (Figure 1). Both provinces consist of linear chains of volcanic islands and seamounts that display a general SW-NE progression of increasing volcanism age, aligning with the movement of the African plate. They are both marked by relatively low-magnitude seismic activity, which on the Canaries is mainly associated with volcanic processes (Carracedo & Troll, 2021). Although still under debate, the volcanism of both archipelagos is attributed to the interaction between the African Plate and underlying mantle plumes (Mata et al., 1998; Geldmacher et al., 2001, 2005; Civiero et al., 2021; Negredo et al., 2022).

The most recent travel-time tomography models image slow anomalies under both archipelagos, attributed to mantle upwellings (Civiero et al., 2018; Civiero, Custódio, et

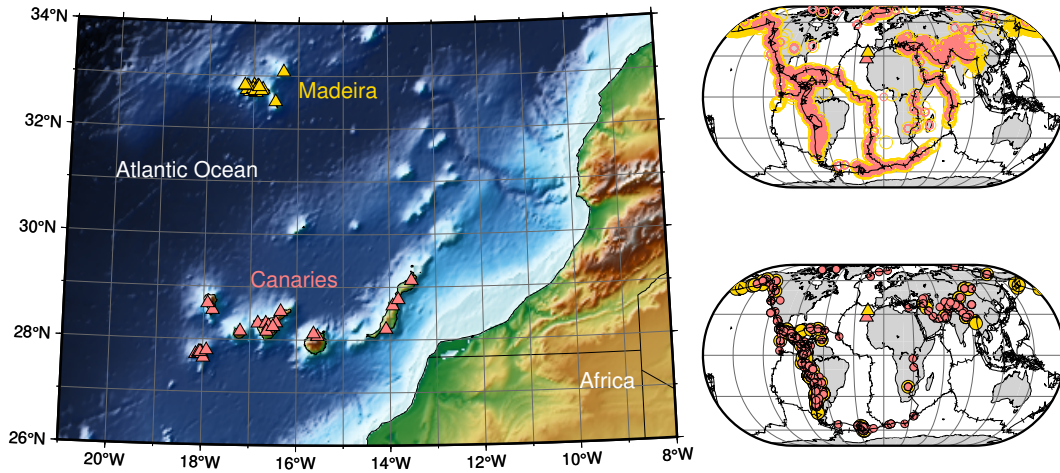


Figure 1. Map of the Canary and Madeira archipelagos displaying station locations (left), with yellow and red triangles representing stations in Madeira and the Canaries, respectively. On the right, the global distribution of all teleseismic earthquakes recorded in the seismic stations (top) and the ones used in the final analysis (bottom) after rigorous quality controls, with red triangles marking the positions of the Madeira archipelago and green for the Canary archipelago. Events follow the same color coding as the triangles, with green indicating events analyzed for the Canaries and red for those related to Madeira.

73 al., 2019). In a recent comprehensive analysis employing tomography and paleo-reconstruction
 74 models, Civiero et al. (2021) proposed that both the Madeira and Canary hotspots are
 75 fed by plume-like structures overlying the seismically slow Central-East Atlantic Anomaly
 76 (CEAA). This anomaly emerges from depths below 700 kilometres and maintains a con-
 77 nection with the African LLSVP (Large Low-Shear-Velocity Province). However, the two
 78 hotspot systems seem to be in different stages of development. According to this model,
 79 while the Canary plume-like structure is rooted in the CEAA, tomography results hint
 80 that the small Madeira plumelet (100 km width) appears detached from it. The plumelet
 81 extends from the surface down to at least 300 km, below which the resolution degrades.
 82 The presence of mantle upwellings beneath the Canary and Madeira archipelagos is also
 83 supported by new shear-wave splitting measurements (Schlaphorst et al., 2022). How-
 84 ever, in the Canary Province many of the predictions of plume theory (Morgan, 1972)
 85 are not met, e.g., volcano ages do not follow a consistent linear age–distance relation-
 86 ship, with coeval volcanism occurring across several hundreds of kilometres (Geldmacher
 87 et al., 2001, 2005). Insights from numerical modelling of mantle flow highlight the po-
 88 tential role of edge-driven convection in deflecting the mantle plume beneath the Canary
 89 archipelago, providing a plausible explanation for the complex age progression of the mag-
 90 matism and widespread volcanism (Negredo et al., 2022; Manjón-Cabeza Córdoba & Ballmer,
 91 2022).

92 Studying the seismic discontinuities beneath both hotspots can provide new insights
 93 into the mantle thermal and compositional properties of these regions, thus allowing the
 94 assessment of the origin of these hotspots. Seismic discontinuities mark discernible changes
 95 in the density, shear and compressional wave speeds of the mantle as depth increases.
 96 The occurrence, depth and seismic visibility of these changes are dependent on the tem-
 97 perature and composition variability of the mantle. The upper mantle has predominantly
 98 peridotite composition, where the dominant mineral is olivine, usually corresponding to
 99 more than 50% volume, accompanied by orthopyroxene and, in most fertile compositions,
 100 by clinopyroxene and an aluminous phase that changes with pressure (e.g., Ziberna et

101 al., 2013, and references therein). This dominant peridotite composition contains dis-
 102 persed eclogite domains, resulting from recycling altered oceanic crust into the mantle
 103 via subduction (e.g., Allègre & Turcotte, 1986; Helffrich & Wood, 2001). Such predom-
 104 inant olivine-rich parageneses change in depth as a result of several phase transitions (PT)
 105 that explain the observations of sharp seismic discontinuities at the base of the upper
 106 mantle: at a depth of 410 km olivine transforms to wadsleyite (ol→wa) with a positive
 107 Clapeyron slope, at 520 km wadsleyite transforms to ringwoodite (wa→ri) with a pos-
 108 itive Clapeyron slope and at 660 km ringwoodite dissociates into bridgmanite ((Mg, Fe)-
 109 perovskite) and magnesiowustite (ri→br+mw) with a negative Clapeyron slope (e.g., Helf-
 110 frich, 2000; Helffrich & Wood, 2001). The corresponding seismic discontinuities are named
 111 410, 520 and 660, after the approximate depth at which the PT occur. The region of the
 112 mantle bounded by the 410 and 660 is known as the Mantle Transition Zone (MTZ).

113 The thermal and compositional structure of the mantle introduces complexities in
 114 the PT. Temperature anomalies in the mantle move the PT to different pressures (depths)
 115 according to their respective Clapeyron slopes (Bina & Helffrich, 1994). Due to the op-
 116 posite sign in the Clapeyron slopes of the PT responsible for the 410 and 660, the depth
 117 changes of these discontinuities are anti-correlated in response to a thermal anomaly. There-
 118 fore, while the 410 becomes shallower in colder regions and deeper in hotter ones, the
 119 depth changes of the 660 are opposite. Consequently, the MTZ is expected to be thicker
 120 when crossed by subducted slabs and thinner in high temperature regions (Vidale & Benz,
 121 1992; Collier & Helffrich, 2001; Helffrich, 2000; Lawrence & Shearer, 2006). This expected
 122 behaviour of the MTZ has been used as an indication of thermal anomalies, akin to a
 123 mantle thermometer (e.g., Helffrich, 2000).

124 Variations in composition and temperature may lead to other mineral phase trans-
 125 formations introducing further complexities in the structure of the MTZ and the man-
 126 tle above. For example, at extremely high temperatures, perovskite may appear at 660-
 127 700 km by a PT involving majorite garnet, which is thought to be, at those conditions,
 128 the dominant mineral phase at the MTZ (Weidner & Wang, 1998; Hirose, 2002; Yu et
 129 al., 2011; Liu et al., 2018). The majorite garnet PT has a positive Clapeyron slope, which
 130 contrasts with the positive slope of the ringwoodite PT. As a result, in a hot mantle, the
 131 660 would occur at greater depths. This could lead to a positively correlated depressed
 132 topography on the 410 and 660 discontinuities with a minor overall impact on the thick-
 133 ness of the MTZ (Deuss et al., 2006; Deuss, 2007). Furthermore, this PT occurs across
 134 a broad depth interval, significantly broadening the 660 discontinuity. Moreover, the role
 135 of aluminum on the stability fields of ringwoodite and majorite garnet has been a sub-
 136 ject of debate (Weidner & Wang, 1998; Yu et al., 2011).

137 Additionally, mantle upwellings rooted deep in the mantle not only exhibit high
 138 temperatures but also different composition from the surrounding mantle. As part of man-
 139 tle convection, cold, ancient oceanic crust is transformed into eclogite in subduction zones,
 140 transported to the lower mantle and then is brought back up into the upper mantle once
 141 entrained in hot mantle plumes. Because of their unique chemical signature, these plumes
 142 are known as thermochemical plumes rather than purely thermal plumes (see Koppers
 143 et al. (2021) for a review). The presence of a consistent seismic discontinuity approxi-
 144 mately 300 km beneath various hotspots is considered strong evidence of the thermo-
 145 chemical nature of deep-seated plumes (Schmerr, 2015; Kemp et al., 2019; Pugh et al.,
 146 2021). This discontinuity named the 300 or X discontinuity, is attributed to the coesite-
 147 to-stishovite (co→st) phase transition in regions of the mantle enriched in eclogite (Williams
 148 & Revenaugh, 2005), as expected for a thermochemical plume.

149 Receiver functions and precursor studies have examined the MTZ beneath the Ca-
 150 nary Islands at a regional scale, while those from Madeira are contributions from global
 151 studies. In the Canaries, studies indicate a thinner MTZ, possibly due to hot mantle ma-
 152 terial (Deuss, 2007; Martinez-Arevalo et al., 2013; Saki et al., 2015). For Madeira, stud-
 153 ies show a moderately thinner MTZ, supporting the plume theory (Houser et al., 2008;

154 Lawrence & Shearer, 2008; Deuss, 2009). However, a detailed analysis of MTZ discon-
 155 tinuities is lacking in both regions, especially for Madeira.

156 In this study, we investigate the fine structure of the upper mantle and MTZ be-
 157 neath both archipelagos using receiver functions. In particular, we estimate the time,
 158 amplitude and frequency content of P-to-s converted phases from which we derived the
 159 depth, magnitude and width of velocity jumps of mantle discontinuities. Through a com-
 160 prehensive interpretation of our findings in the context of mineral physics and geody-
 161 namics, we inferred the thermochemical nature of the Canary mantle plume. Beneath
 162 Madeira, our findings confirm the observations from Civiero et al. (2021) suggesting that
 163 the plume appears to be disconnected from the lower mantle and primarily affects the
 164 upper portion of the MTZ.

165 2 Data

166 For the Canary archipelago, we use data from 23 stations of the Spanish Digital
 167 Seismic Network (operated by the *Instituto Geográfico Nacional*) and one station from
 168 the Global Seismograph Network. These stations were active in varying periods, rang-
 169 ing from 2008 to 2017. For Madeira, we use data from 16 stations from the temporary
 170 DOCTAR network that was active during 2011/2012 (Matos et al., 2015), as well as 2
 171 permanent stations of the Portuguese National Seismic Network (Instituto Português do
 172 Mar e da Atmosfera, I.P., 2006). of those stations are short-period, so we removed the
 173 instrument response before the processing. See Figure 1 for station deployment and Ta-
 174 ble S1 in the supporting material for names and geographic coordinates of stations.

175 We selected the waveforms of 1241 events for the Canary archipelago and 1268 events
 176 for Madeira, of Mw between 5.5 and 7 and from epicentral distances between 30° and
 177 95° . After discarding incomplete ZNE triplets, we obtain 13578 three-component wave-
 178 forms for the Canary archipelago and 6481 for Madeira.

179 3 Method

180 To investigate the structure of the upper mantle, we employ receiver functions (RFs)
 181 and common conversion point stacking techniques.

182 3.1 Receiver functions

183 We use teleseismic *Pds* phases, i.e. the phases resulting from the direct *P* wave con-
 184 verting to an *S* wave at a seismic discontinuity at a depth *d*. Because of their polariza-
 185 tion and their almost vertical incidence, *Pds* conversions are recorded on the radial (*R*)
 186 component of teleseismic earthquakes. The direct detection of *Pds* phases in individual
 187 seismograms is challenging due to their weak amplitude and their arrival during the coda
 188 of the *P* phase, which is marked by numerous other phases, including multiple reflections
 189 and scattered waves. However, converted phases are expected to be coherent with the
 190 waveform of the main *P* arrival for conversion at discontinuities which are thinner than
 191 one-half of the *P*-wavelength (Richards, 1972; Paulssen, 1988; Bostock, 1999). There-
 192 fore, it is possible to extract them by waveform similarity. This can be done using de-
 193 convolution of the *P* phase in the vertical component (*P_Z*) from *R*, which is known as
 194 the receiver function (RF) technique (Phinney, 1964; Vinnik, 1977; Langston, 1979; Am-
 195 mon, 1991). The deconvolution process eliminates the source component and isolates the
 196 P-to-s conversion peaks from discontinuities beneath the station.

197 We compute RFs using the processing methods outlined in Bonatto et al. (2015,
 198 2020). The processing workflow is illustrated in Figure 2a and described in detail in Sup-
 199 porting material Section 1. After the processing and the quality controls, we obtain 948
 200 RFs for the Canaries and 320 RFs for the Madeira archipelago in five frequency bands:

201 0.02-0.12 Hz, 0.02-0.2 Hz, 0.02-0.32 Hz, 0.02-0.48 Hz, 0.02-0.64 Hz. Table S1 summarises
 202 the number of teleseismic records per station and the corresponding final number of good-
 203 quality RFs.

204 3.2 Stacking of receiver functions with moveout correction

205 During the stacking process, we apply a linear moveout correction, also known as
 206 a slowness stack, to account for the time delay between the arrival of seismic waves at
 207 different distances from the source. This correction ensures that the seismic signals are
 208 accurately aligned and stacked, resulting in improved signal detection and identification.

209 To perform the stacking process with a linear moveout correction, we use two tech-
 210 niques: the phase weighted stack (PWS) (Schimmel & Paulssen, 1997) and the linear stack
 211 (LS). The PWS is a non-linear stacking technique that incorporates the coherence of the
 212 instantaneous phase as a weight in the linear stack, enhancing the signal-to-noise ratio
 213 (SNR) and improving the accuracy of signal detection.

214 The stacking process with moveout correction, accounting for both stacking tech-
 215 niques, is applied as follows:

$$S(s_j, t) = \frac{1}{N} \sum_{i=1}^N RF_i(t + s_j(\Delta_i - \Delta_{REF}))c_i \quad (1)$$

216 where s_j refers to a specific relative slowness with respect to the P phase, t is relative
 217 time with respect to the P phase, Δ_i is the epicentral distance for RF_i , Δ_{REF} is the ref-
 218 erence epicentral distance, and N is the total number of stacked RFs. The reference dis-
 219 tance, Δ_{REF} , of 75° is chosen for all the slowness stacks to account for the distribution
 220 of epicentral distances which are mainly concentrated between 60° and 90° .

221 The weight c_i in equation 1 is the phase stack and it accounts for the instantaneous
 222 phase similarity:

$$c_i = \left| \frac{1}{N} \sum_{k=1}^N e^{i\phi_k(t+s_j(\Delta_i-\Delta_{REF}))} \right|^\nu \quad (2)$$

223 ϕ_k is the instantaneous phase for the k -th RF, and the parameter ν controls the weight-
 224 ing of phase similarity and dissimilarity. The move-out corrected LS is defined with $\nu =$
 225 0 ($c_i = 1$), while for the PWS we choose a value of $\nu = 2$.

226 3.2.1 Identification of converted phases in global stacks

227 The average fine structure of the upper mantle in the study area is obtained by stack-
 228 ing all the RFs that passed the quality controls in the lowest frequency band (0.02–0.12
 229 Hz). This global stack is useful for identifying converted phases from major discontinu-
 230 ities and from minor reflectors that are prevalent throughout the area.

231 Figures 3 a and b display relative time-distance stacks of RFs for the Canaries and
 232 Madeira datasets, respectively, with the P phase set as time zero. Each trace at a given
 233 epicentral distance is computed from the stack (PWS) of RFs with epicentral distances
 234 within a 5° interval and uses a fixed relative slowness parameter of -0.1 s° to perform
 235 the move-out correction within that distance interval. Since converted phases have a steeper
 236 angle of incidence than the direct P phase, Pds phases are always expected to align along
 237 a negative slope line (i.e., negative relative slowness), as shown with the continuous black
 238 lines. Conversely, multiples have a shallower angle of incidence and a corresponding pos-
 239 itive slope (i.e., positive relative slowness), as shown with the dashed lines. Slowness stacks,

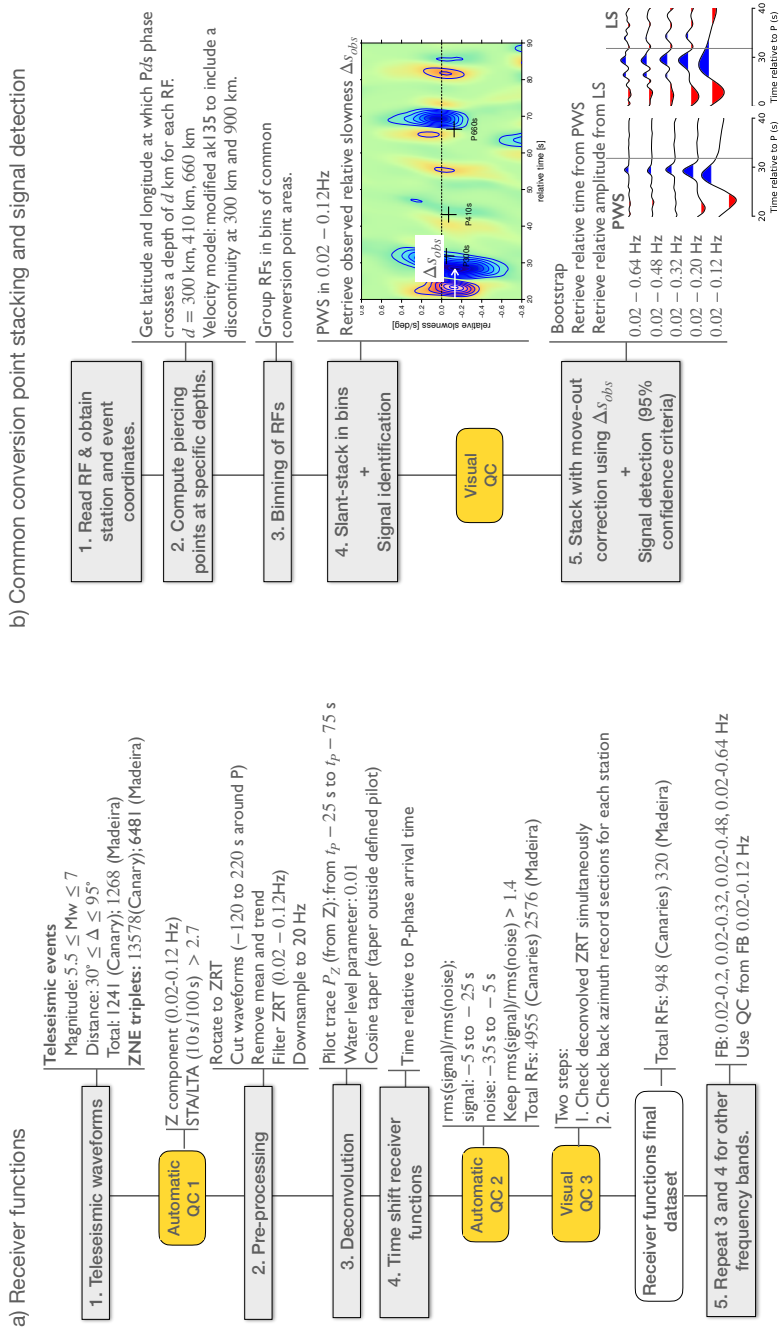


Figure 2. Processing workflow of a) Receiver functions and b) Common conversion point stacking of RFs.

240 also referred to as vespagrams or relative time-slowness stacks, are a useful tool for un-
 241 ambiguously identifying *Pds* phases. Figure 3 c and e show the slowness stacks for the
 242 Canary dataset and Figure 3 d and f show the slowness stack for the Madeira dataset.
 243 Here, all RFs are stacked applying a linear move-out correction for a range of slowness
 244 values and the result is plotted in the relative time-slowness domain, where the refer-
 245 ence at zero is the *P* phase. Conversions from discontinuities in the upper mantle are
 246 expected with negative relative slowness, while multiples are expected with positive rel-
 247 ative slowness.

248 **3.2.2 Common conversion point stacking and signal detection**

249 The lateral variations of the detected discontinuities are investigated using a common-
 250 conversion-point (CCP) stacking approach as in Bonatto et al. (2020). The processing
 251 workflow for the CCP stacking and signal detection is illustrated in Figure 2b. We first
 252 retrieve station and event coordinates for each RF (step 1, Figure 2b) and compute pierc-
 253 ing points of converted phases *P300s*, *P410s* and *P660s* at their respective conversion
 254 depths: 300 km, 410 km, and 660 km (step 2, Figure 2b). The CCP stacking is performed
 255 for these three conversion depths, which correspond to the reference depth of our tar-
 256 get discontinuities. For each conversion depth, we stack the RFs with conversion point
 257 coordinates in the same circular area or bin (step 3, Figure 2b). To ensure reliable mea-
 258 surements, we set the bin radius at each conversion depth to match the size of the first
 259 Fresnel Zone at an intermediate frequency of 0.2 Hz: $r_{P300s,P410s} = 0.5^\circ$ and $r_{P660s} =$
 260 0.75° . The centres of these bins are spaced equally at intervals of 0.7° to enable an over-
 261 lap of the sampled areas. Notice that even with the smallest bin radius of 0.5° , the 0.7°
 262 interval permits an intentional overlap of 0.3° . If the number of RFs in the bin is less
 263 than 25, we increase the bin radius to $r_2 = 1.5r_{Pds}$, or to $r_3 = 2r_{Pds}$ if numbers re-
 264 main low. After stacking the RFs in each bin and conversion depth, we perform a visual
 265 quality assessment of individual slowness stacks within the lowest frequency band of 0.02–
 266 0.12 Hz (step 4, Figure 2b). We allocate a quality level from 1 to 3 for each stack, based
 267 on these criteria:

- 268 1: The signal identification is very clear, without other signals near the target phase.
- 269 2: Other coherent signals near the target phase, but the signal is still clear.
- 270 3: Multiple coherently stacked signals of similar amplitude near the target signal or
 271 non-detection.

272 Representative examples of stacks classified as quality 1, 2, and 3 for *P300s* are shown
 273 in Figs. S1 to S11 of Supporting material Section 2. Stacks with quality 1 and 2 are con-
 274 sidered as good quality stacks and stacks of quality 3 are not considered in the analy-
 275 sis.

276 We use the good quality stacks to estimate the relative slowness at which each phase
 277 is detected. Then, for each frequency band (0.02-0.12 Hz, 0.02-0.2 Hz, 0.02-0.32 Hz, 0.02-
 278 0.48 Hz, 0.02-0.64 Hz), we compute the stacking with move-out correction (step 5, Fig-
 279 ure 2b) using this slowness value; i.e., fixed s_j in Eq. 1. The final stacks are calculated
 280 using a bootstrap resampling algorithm of 20 repetitions with replacement (i.e., a wave-
 281 form may be chosen multiple times). The bootstrap method enhances our statistical anal-
 282 ysis. This approach involves constructing a distribution of stacked RFs for each CCP
 283 bin by resampling and stacking numerous subsets of data. This approach fulfils two key
 284 objectives: first, it mitigates the influence of outliers by diluting the effect of any indi-
 285 vidual RF with an anomalously large amplitude across multiple bootstrap iterations. Sec-
 286 ond, it promotes the reliable detection of any consistent feature within the stacks, re-
 287 gardless of its magnitude. The recurrence of any distinctive pattern within the bootstrap
 288 samples strongly indicates the presence of a genuine geophysical feature, rather than merely
 289 being the result of data variability. Moreover, this method enables us to perform a thor-
 290 ough evaluation of the statistical significance of the RF amplitude observations.

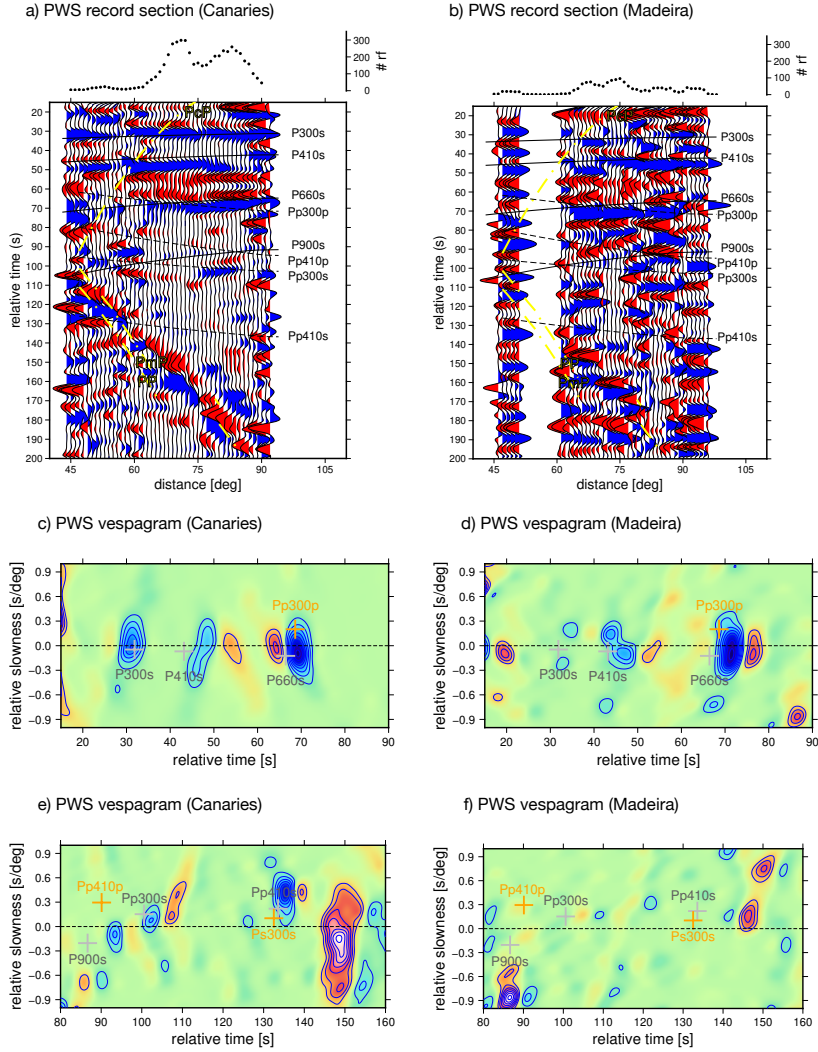


Figure 3. Record sections for (a) the 948 RFs from the Canary Island dataset and (b) the 320 RFs from the Madeira dataset. Each trace in the record sections results from stacking (PWS) the RFs with epicentral distances within a 5° interval around a given epicentral distance in the horizontal axis. Blue and red colours represent positive and negative amplitudes. Black lines show the theoretical travel time curves for a slightly modified ak135 reference model that includes imperceptible density increase at 300 km and 900 km. Dashed yellow lines represent travel time curves for potentially interfering phases (PcP, PmP, PP). The number of RFs is indicated at the top of the record section. (c)-(f) Stacking (PWS) in the relative time-slowness domain for the Canary and Madeira dataset in different time intervals. Crosses mark the expected time and slowness of different phases for positive (gray) and negative polarities (orange) in the modified ak135 reference model.

291 We measure the relative travel time values from the PWS and the amplitude of con-
 292 verted phases from the LS. We only include signals in the analysis that meet the 95%
 293 confidence criteria, which requires the amplitude of a detected signal to be at least twice
 294 its amplitude standard error. Finally, we retain only those detected signals from good-
 295 quality stacks (quality levels 1 and 2) with more than 25 stacked RFs. These detections
 296 should also show negative slowness and positive amplitude, as expected for the target-
 297 converted phases.

298 3.3 Time-to-depth conversion

299 To convert relative times to depth, we use tomography-derived velocities. Veloc-
 300 ity anomalies are extracted from two tomography models: the global model MIT08 (Li
 301 et al., 2008) and the regional model IBEM-P18 (for P waves)/IBEM-S19 (for S waves)
 302 (Civiero et al., 2018; Civiero, Custódio, et al., 2019). While the regional model has a higher
 303 resolution, it does not cover the entire area of interest. However, we include it in the anal-
 304 ysis to assess the consistency of the results in the overlapping region with both models.
 305 Since MIT08 only accounts for P-wave anomalies, we approximate corresponding S-wave
 306 anomalies to be 1.3 times P-wave anomalies at the surface, increasing linearly to 3 times
 307 at the base of the mantle, following Ritsema and Van Heijst (2002). To account for possi-
 308 ble resolution overestimation given by noiseless synthetic tests (Li et al., 2008; Civiero,
 309 Armitage, et al., 2019), we assume that the amplitudes of anomalies recovered by the
 310 inversion could be about 50% than those of unknown real anomalies. Therefore, we com-
 311 pute the corrections using MIT08 and IBEM-P18/S19 anomalies multiplied by a factor
 312 of 2.

313 For each tomography model, we compute time corrections for each CCP bin and
 314 converted phase. We use TauP toolkit (Crotwell et al., 1999) to create a modified *ak135*
 315 velocity model for each bin which includes the anomalies. We use this new velocity model
 316 to compute the theoretical relative travel times of converted phases (for a reference dis-
 317 tance of 75°). Then, we use these relative travel times to compute time corrections with
 318 respect to *ak135*, i.e., the difference between travel times obtained with *ak135* and with
 319 the modified *ak135*. Finally, we add the correction to the observed relative times of de-
 320 tected signals and the corrected time values are converted to depth using the reference
 321 velocity model *ak135* for a reference distance of 75° . Although the tomographic mod-
 322 els used to compute the corrections have large uncertainties, it should be noted that the
 323 overall effect of the corrections is to locate the discontinuities closer to their actual depth.

324 3.4 Temperature variations in the MTZ

325 The thickness of the MTZ at each location is calculated by subtracting the depths
 326 of the 410 and 660 discontinuities ($z_{660} - z_{410}$). Variations in the MTZ thickness can
 327 be attributed to temperature variations, as thermal anomalies affect the depths of the
 328 410 and 660 discontinuities differently.

329 The conversion of anomalous MTZ thickness to temperature is accomplished through
 330 the use of Clapeyron slopes associated with the olivine phase transitions (refer to Ta-
 331 ble S2). Clapeyron slopes (dP/dT or γ) can be written as

$$\left(\frac{dP}{dT}\right)_H \approx \frac{dP}{dz} \frac{\delta z_H}{\delta T} \quad (3)$$

332 where H stands for 410 or 660, δz_H corresponds to $\delta z_{410} = 410 - z_{410}$ or $\delta z_{660} = 660 -$
 333 z_{660} and dP/dz is the upper-mantle pressure increase with depth which is about $100/3$
 334 MPa km^{-1} in *PREM* (Dziewonski & Anderson, 1981).

335 As proposed by Helffrich (2000), we adopt the assumption that the deflection of
 336 discontinuities is due to vertically consistent temperature changes. Therefore, we can con-
 337 vert the difference in MTZ thickness to temperature variation using the equation below

$$\delta T = \left[\left(\frac{dP}{dT} \right)_{660} - \left(\frac{dP}{dT} \right)_{410} \right]^{-1} \frac{dP}{dz} \delta MTZ \quad (4)$$

338 where $\delta MTZ = MTZ_{thickness} - 250$ km or $\delta MTZ = MTZ_{thickness} - 242$ km, if we
 339 consider the reference value for the MTZ thickness from the global RFs study of Lawrence
 340 and Shearer (2006).

341 **3.5 Frequency and amplitude analysis of converted phases**

342 Studying the seismic visibility and the amplitude of seismic phases provides im-
 343 portant constraints on the sharpness and velocity contrast of the velocity gradients as-
 344 sociated with mantle discontinuities. (Shearer & Flanagan, 1999; van der Meijde et al.,
 345 2003; Juliá, 2007; Bonatto et al., 2020; Pugh et al., 2021). These parameters and the dis-
 346 continuity depth are directly linked to the underlying mechanisms that give rise to the
 347 seismic boundaries and play an important role in interpreting our observations.

348 **3.5.1 Sharpness of discontinuities**

349 Seismic discontinuities are generally approximated as linear velocity gradients, which
 350 act as a low pass filter to converted waves. In particular, the amplitudes of the converted
 351 waves at the discontinuity are significant when the gradient transition interval, Δz , is
 352 smaller than half of the wavelength, λ_P , of the incident P -wave (Bostock, 1999; Paulssen,
 353 1988). This is

$$\Delta z < \frac{\lambda_P}{2} = \frac{v_P}{2f} \quad (5)$$

354 where v_p is the P -wave velocity at the corresponding discontinuity depth. Therefore, to
 355 constrain the thickness of discontinuities, we need to find the highest frequency f^{max}
 356 for which the amplitude of converted phases is visible. We estimate this frequency value by
 357 analyzing the amplitudes of converted phases in the CCP linear stacks across the dif-
 358 ferent frequency bands that we use to compute the RFs. We use the following criteria:
 359 f^{max} is the frequency above which the amplitude drops below 50% of the amplitude at
 360 the lowest frequency. Finally, the upper bound for the thickness of the discontinuity is
 361 obtained by substituting f with f^{max} in Eq. 5. This rule of thumb has been used be-
 362 fore to constrain the thickness of mantle discontinuities (e.g., Paulssen, 1988; Bostock,
 363 1999; van der Meijde et al., 2003; Jenkins et al., 2017; Bonatto et al., 2020).

364 **3.5.2 Velocity contrast**

365 Reflection and transmission coefficients describe how the energy of a seismic wave
 366 is partitioned when it encounters a boundary between two elastic media. They are ob-
 367 tained as the amplitude ratio of the incoming wave and the reflected or transmitted waves.
 368 The coefficients depend on several factors, including the velocities and densities of the
 369 seismic waves on both sides of the interface (the velocity and density contrasts), and the
 370 angle of incidence of the incoming wave. The elementary formulas to compute the co-
 371 efficients can be found in equations 5.39 and 5.40 of Aki and Richards (2002).

372 To estimate the velocity contrast across each detected discontinuity, we manually
 373 compare the theoretical coefficients of converted phases, assuming different velocity con-
 374 trasts, with the estimated amplitudes of the Pds phases in our stacked RFs. This com-
 375 parison allows us to obtain a rough assessment of the velocity jump. To minimize atten-

376 uation effects due to the finite thickness of discontinuities, we perform this analysis for
 377 RFs in the lower frequency band: 0.02-0.2 Hz. In this approach, we assume that *Pds* phases
 378 are primarily sensitive to S-wave velocity contrasts, as demonstrated by Juliá (2007).

379 4 Results

380 We investigate the upper mantle and MTZ structure using 948 high-quality RFs
 381 around the Canaries and 320 around Madeira. We first create time-distance stacks and
 382 vespagrams for the entire dataset of each archipelago to identify converted phases of pos-
 383 sible discontinuities prevalent throughout the area.

384 The number of events observed at stations in the Canary archipelago that pass the
 385 quality controls are higher across almost the entire distance range, resulting in stronger
 386 signals of the major converted phases in the time-distance stacks (Figures 3 a, b). The
 387 vespagrams confirm that we obtain clear converted phases from the globally detected 410
 388 and 660 discontinuities beneath both volcanic provinces (Figures 3 c, d). However, a clear
 389 converted phase at a reflector near 300 km depth is only observed beneath the Canaries.
 390 Based on the robust detections of the 410 and 660, we have confidence that this mea-
 391 surement of the X discontinuity is not an anomaly caused by data coverage. In contrast
 392 to the Canary archipelago, no strong multiples (Pp300s and Pp410s) from the reflectors
 393 at the X and 410 discontinuities can be observed around the Madeira archipelago (Fig-
 394 ures 3 e, f). Likewise, a converted phase at a discontinuity of approximately 800-900 km
 395 depth can be observed around the Canaries but is not present around Madeira. This phe-
 396 nomenon will be subject to further investigation in a future study.

397 4.1 Topography of discontinuities and MTZ thickness

398 To investigate the spatial distribution of the converted phases, we apply the CCP
 399 stacking method. Figure 4 shows the CCP bins where converted phases were reliably de-
 400 tected. Then, we use the relative times of the converted phases to estimate the depth
 401 of the discontinuities from tomography-derived velocities with the global model MIT08
 402 (Li et al., 2008).

403 Our analysis indicates that the X discontinuity is situated at a mean depth of 288 ± 6
 404 km ($\bar{x} \pm 1\sigma_{\bar{x}}$) beneath the Canaries (Figure 5), with a range spanning from 251 km to
 405 316 km. It is prominent around the western and central part of the Canaries with depths
 406 shallower than 300 km towards the south and deeper than 300 km towards the north (Fig-
 407 ure 6a), likely stemming from a larger azimuthal coverage from the west and south. For
 408 Madeira, we have only retained one reliable detection of this discontinuity in the west,
 409 with a depth of 313 km.

410 On average, the 410 is located deeper beneath the Canaries (Figure 5) with a mean
 411 depth of 428 ± 4 km and a range of 403 km to 448 km, in comparison to a mean depth
 412 of 421 ± 3 and a range of 407 km to 428 km beneath Madeira. Whereas in the Canaries
 413 it is located deeper towards the western part of the archipelago with values larger than
 414 410 km southwest of the islands of La Palma, Tenerife and Gran Canaria, and smaller
 415 values to the northeast, a lateral trend is not as evident around the Madeira archipelago
 416 (Figure 6 b). This difference can be attributed to Madeira's smaller geographical extent
 417 compared to the Canaries, as well as the fact that the stations collectively cover a sig-
 418 nificantly smaller area. We observe, larger values in the northwest and a shallower value
 419 towards the south, making this pattern less pronounced.

420 In contrast, the 660 is shallower towards the east of the Canary archipelago with
 421 a mean depth of 647 ± 2 km and ranges of 625 km to 675 km, in comparison to a mean
 422 depth of 664 ± 3 km and a range of 637 km to 687 km beneath Madeira. Based on the
 423 piercing point distribution, nearly all results can be found towards the west of Madeira

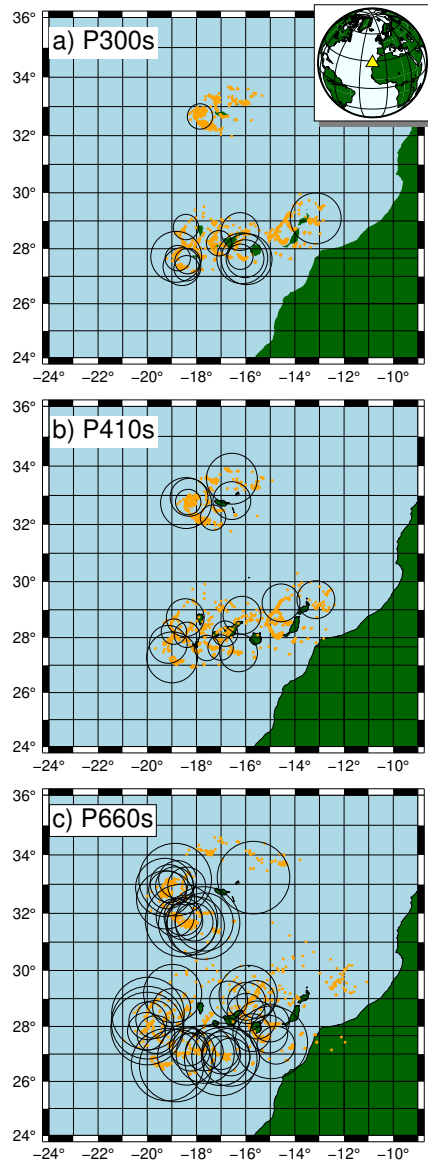


Figure 4. Location of common conversion point bins with robust detections (with PWS and LS) of the converted phases: a) P300s, b) P410s, and c) P660s. Circles correspond to CCP bins with signals that satisfy the 95% confidence criteria. The size of the circles are proportional to the radius of the CCP bin; from the smallest to the largest, the radii of the circular sectors are: 0.5° , 0.75° , 1.0° , 1.25° , 1.5° . Orange dots indicate the piercing points of corresponding phases.

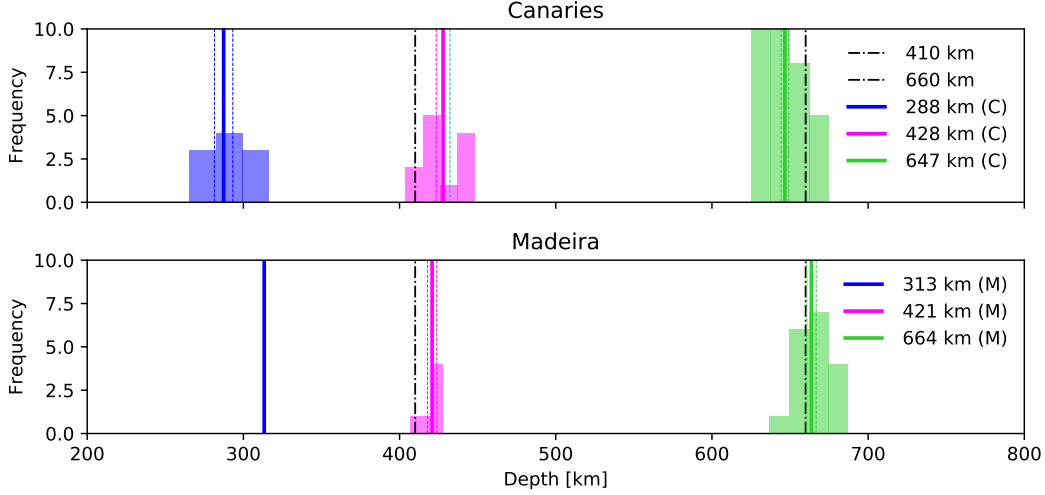


Figure 5. Histograms of estimated depth values, after time corrections, for the X, 410, and 660 discontinuities beneath the Canaries and Madeira. Vertical solid lines (blue, pink, green and black) correspond to mean depth values for both archipelagos (given in the legend, where M stands for Madeira and C for the Canaries), dashed lines correspond to standard errors of mean values and dash-dotted lines are reference depth values in a modified ak135 model that incorporates a discontinuity at 300 km.

424 and around the western and central part of the Canaries (Figure 6c). In Madeira, the
 425 660 is detected at larger depths towards the west, whereas it is shallower towards the
 426 east. The opposite colour scales for the 410 km and 660 km depth maps were deliberately
 427 selected to visually represent the relationship between depth and temperature.

428 The general trend of a deeper 410 and a shallower 660 in the Canaries results in
 429 a thinner MTZ there at 216 ± 2 km compared to 237 ± 2 km around Madeira (Figures 6
 430 d). These MTZ thickness values are derived from depth estimates of the 410 and 660 dis-
 431 continuities, constrained to regions where observations for both discontinuities are avail-
 432 able.

433 4.2 Sharpness and velocity contrast of detected discontinuities

434 Figure 7 shows the average amplitudes of the $P300s$, $P410s$, and $P660s$ phases relative
 435 to P across five frequency bands for both archipelagos. As expected for linear ve-
 436 locity gradients, the amplitude of all converted phases decreases with higher upper-frequency
 437 boundaries. We apply the criteria defined in section 3.5 to constrain the thickness of the
 438 discontinuities. In the Canary archipelago, $P300s$, $P410s$, and $P660s$ exhibit an ampli-
 439 tude reduction of $\sim 50\%$ (w.r.t the lowest frequency band) at 0.64 Hz. Therefore, we con-
 440 sider $f^{max} = 0.64$ Hz for all converted phases, indicating that the detected disconti-
 441 nuities are sharp. Using Eq. 5 and corresponding values of v_p in ak135, we obtain $\Delta z_{300,Can} <$
 442 7 km, $\Delta z_{410,Can} < 7$ km, and $\Delta z_{660,Can} < 8$ km. In Madeira, $P300s$ exhibits an ampli-
 443 tude drop of $\sim 50\%$ at 0.64 Hz, $P410s$ is still over 50% at 0.64 Hz. These results lead
 444 to sharp discontinuities: $\Delta z_{300,Mad} < 7$ km, $\Delta z_{410,Mad} < 7$ km (or even sharper). For
 445 $P660s$, the maximum frequency for which significant energy is converted is 0.48 Hz, which
 446 corresponds to $\Delta z_{660,Mad} < 11$ km.

447 In both archipelagos, the amplitude of $P300s$, $P410s$, and $P660s$ relative to P de-
 448 creases gradually with increasing frequencies, shifting from average values of approxi-

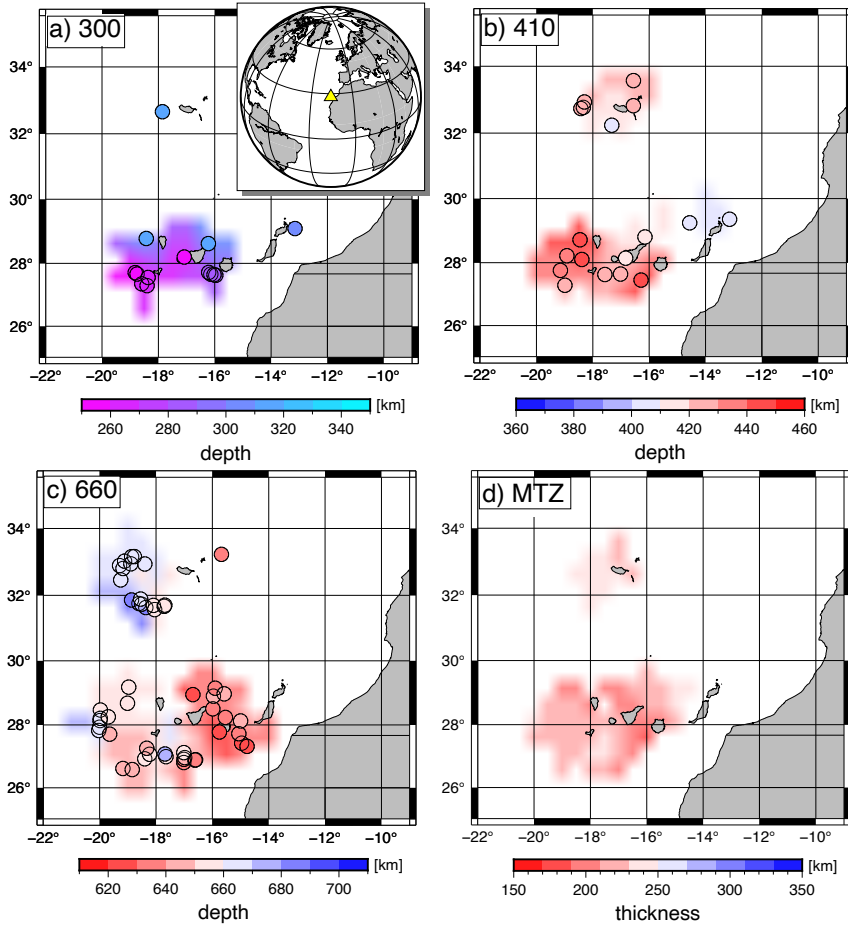


Figure 6. Maps showing discontinuity depth (a, b, c) and MTZ thickness surfaces (d), derived from depth estimates of the 410 and 660 discontinuities, constrained to regions where observations for both discontinuities are available. Circles with thicker lines correspond to robust detections in the PWS and LS, i.e., signals that satisfy the 95% confidence criteria. The ones with a thinner line correspond to robust detection only in the LS (the signal is visible in the PWS but it does not satisfy the 95% confidence criteria).

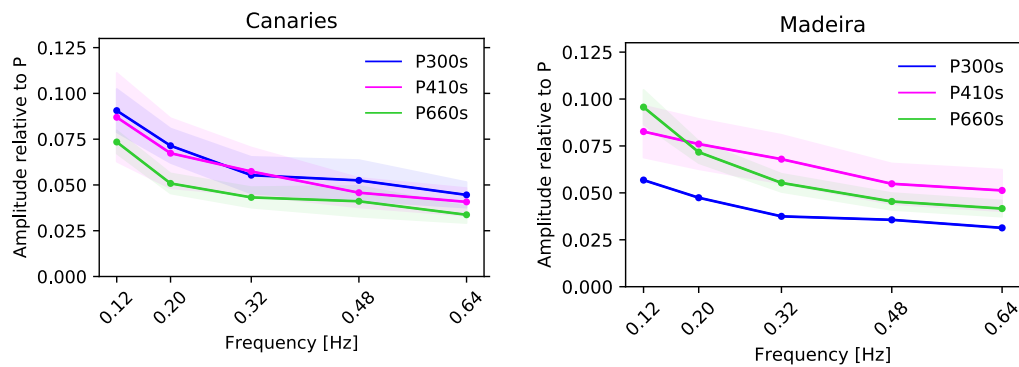


Figure 7. Change of relative amplitude of converted phases for different higher cut-off frequencies for the Canary (left) and Madeira (right) archipelagos. Values are given as a fraction of the initial *P*-phase amplitude. The shaded areas show uncertainties. Note, that *P*300s in Madeira consists of only one measurement.

	phase	averaged observed amplitude ± 2 st err at 0.2 Hz	theoretical coefficients	v_S jump [%]	relative v_S jump 410/300	410/660
<i>Madeira</i>					1.6	1.1
	P300s	0.047 \pm 0.012	0.047 \pm 0.001	5.1		
	P410s	0.076 \pm 0.027	0.076 \pm 0.002	8.1		
	P660s	0.072 \pm 0.012	0.072 \pm 0.002	7.6		
<i>Canaries</i>					0.96	1.3
	P300s	0.072 \pm 0.017	0.071 \pm 0.002	7.6		
	P410s	0.067 \pm 0.038	0.067 \pm 0.002	7.3		
	P660s	0.051 \pm 0.011	0.051 \pm 0.002	5.5		

Table 1. Averaged observed amplitudes and theoretical coefficients used to constrain the velocity jumps (v_S jump) at target discontinuities. Theoretical coefficients are computed by averaging the transmission coefficients across a range of epicentral distances from 60° to 90° .

449 mately 0.09 to 0.04 (Figure 7). Amplitude variability is evident within individual bins
450 across different frequencies, illustrating a consistent decreasing trend in amplitude (Fig-
451 ure S12). However, whereas the amplitude of *P300s* is close to the amplitude of *P410s*
452 across all frequency bands in the Canaries (0.09 ± 0.01 at 0.02-0.12 Hz to 0.04 ± 0.01 at
453 0.02-0.64 Hz), it is the weakest around the Madeira archipelago (0.06 ± 0.02 at 0.02-0.12
454 Hz to 0.03 ± 0.01 at 0.02-0.64 Hz). This discrepancy is further emphasized by the fact that
455 only one robust measurement of this discontinuity could be obtained there. Our observed
456 relative amplitudes at 0.02-0.20 Hz for the Canary and Madeira archipelagos are displayed
457 in Table 1. This specific frequency band was chosen because, at lower frequencies, the
458 effects of the transmission coefficient response due to a velocity gradient on amplitudes
459 are minimized. The table also shows the estimated velocity jumps and their correspond-
460 ing theoretical transmission coefficients.

461 5 Discussion

462 5.1 Uncertainties in time observations

463 Uncertainties in our time detections are related to the smearing of the signal, which
464 is attributed to several factors. First, it is related to the resolution in time, which is frequency-
465 dependent. Moreover, additional complexities arise from random noise, the application
466 of the linear move-out approximation, and the non-homogeneous distribution of epicen-
467 tral distances. Each of these elements contributes to the smearing of signals in vesp-
468 grams. To assess and quantify time uncertainty in individual bins, we use the bootstrap
469 method to estimate a time standard deviation for each detection. We found that on av-
470 erage the time uncertainty for the frequency band 0.02-0.2 Hz is 1.3 ± 0.2 seconds. This
471 corresponds to an average depth uncertainty of about 11 ± 1 km. These values are not
472 surprising when considering that seismic discontinuities are not strictly first-order dis-
473 continuities, as evidenced in the amplitude-frequency analysis. The thickness of the 410
474 and 660 discontinuities (typically on the order of 10 kilometers) imposes limitations on
475 our time and depth resolution. Moreover, a velocity gradient in the Earth's upper man-
476 tle modulates seismic wave travel times across different frequencies (Helffrich & Bina,
477 1994; Bostock, 1999), with high-frequency converted waves experiencing more pronounced
478 delays due to the gradual transition in wave speed (Bostock, 1999).

479 **5.2 Robustness analysis of observed 420 and 660 topography**

480 The absolute depth of discontinuities is determined by the velocity model used to
 481 correct the observed times. Incorrect determination of time corrections could lead to an
 482 inaccurate estimation of the depth of discontinuities. In Supporting material Section 3,
 483 we examine the time corrections and the depth correlations between the topography of
 484 the 410 and 660 discontinuities for both tomographic models, IBEM-P18/-S19 and MIT08,
 485 to assess the accuracy of our time-to-depth conversions. Based on this analysis, we con-
 486 clude that MIT-P08 likely places the 410 and 660 discontinuities slightly deeper than their
 487 true depths. Conversely, the MTZ thickness remains unaffected by the mantle structure
 488 above it. The MTZ thickness is primarily influenced by the internal structure of the MTZ,
 489 characterized by smaller anomalies and consequently smaller errors. This is evident in
 490 Figure S14, showing similar time corrections for the *P410s* and *P660s*.

491 **5.3 Mantle transition zone in the Canary and Madeira archipelagos**

492 **5.3.1 Previous studies**

493 A thinned MTZ has been found beneath the Canary and Madeira archipelagos in
 494 previous studies using RFs and SS/PP precursors. The effect is more pronounced (~ 15 –
 495 20 km thinner than the global average) beneath the Canaries (e.g., Li et al., 2003; Deuss,
 496 2007; Gu et al., 2009; Martinez-Arevalo et al., 2013; Saki et al., 2015), but still evident
 497 beneath Madeira (e.g., Houser et al., 2008; Lawrence & Shearer, 2008; Deuss, 2009). There
 498 are different interpretations for the thinning of the MTZ. Whereas some studies explain
 499 those anomalies through the presence of hot mantle material, thus supporting the the-
 500 ory of existing plumes (e.g., Gu et al., 2009), other studies find that the thinning is sim-
 501 ilar to the widespread thinning of the MTZ beneath oceans observed from SS precur-
 502 sor studies; this thinning is not solely restricted to plumes (e.g., Li et al., 2003; Martinez-
 503 Arevalo et al., 2013).

504 The study of Civiero et al. (2021), based on results from high-resolution seismic
 505 tomography (Civiero et al., 2018; Civiero, Custódio, et al., 2019), shear-wave splitting
 506 (Schlaphorst et al., 2022) and gravity (Sandwell et al., 2014) along with plate reconstruc-
 507 tion showed that the Madeira and Canary volcanism is fed by plume-like structures over-
 508 lying the seismically slow Central-East Atlantic Anomaly (CEAA) developing as a dome-
 509 like instability beneath 700 km depth in connection to the African LLSVP. However, the
 510 two hotspot systems seem to be in different stages of development. While the Canary
 511 plume-like structure is still rooted in the CEAA, tomography results suggest that the
 512 Madeira plumelet is presently detached from it, extending from the surface down to at
 513 least 300 km depth (below which the resolution degrades), which was interpreted as a
 514 result of the Madeira plumelet being probably at a dying stage.

515 **5.3.2 Our study**

516 Our results support and reinforce the presence of a hot rising upwelling beneath
 517 the Canary Islands that extends through the MTZ in agreement with the interpretation
 518 of Civiero et al. (2021). We find that the MTZ is thinner in the Canary archipelago (Fig-
 519 ure 6). This is attributed to a depressed 410 and an uplifted 660, which is consistent with
 520 the MTZ being crossed by a hot mantle upwelling. The negative correlation observed
 521 between the depths of the 410 and 660 discontinuities beneath the Canary Islands con-
 522 firms that the polymorphs olivine and ringwoodite are the dominant minerals influenc-
 523 ing the topography of both discontinuities.

524 In Madeira, the MTZ is also thinner, primarily due to a depressed 410 and a stan-
 525 dard 660, suggesting that the thermal anomaly predominantly affects the 410 disconti-
 526 nuity. This is compatible with a low-velocity anomaly elongating downward to the top
 527 of the MTZ, i.e. extending more than 100 km deeper than the bulk of the anomaly im-

aged in the model by Civiero et al. (2021). The hypothesis of a possible deeper extension of the Madeira plumelet was admitted by the authors, based on considerations about the size of the anomaly and the coarser model resolution below this area. Our results provide complementary information that reinforces the hypothesis that the plumelet extends deeper than 300 km, but does not fully cross the MTZ beneath Madeira and is detached from the CEEA.

Additionally, we observe a lateral trend in the topography of discontinuities, which is more pronounced in the Canary archipelago. The 660 is shallower towards the east, while the 410 is deeper towards the west (Figure 6). Beneath Madeira, the 660 is shallower towards the east; however, this trend is less reliable here due to only one detection to the east of the archipelago. This lateral trend might indicate a lateral deflection of the plume. Numerical modelling of mantle flow highlights the potential role of edge-driven convection in the African craton in deflecting the mantle plume beneath the Canary archipelago towards the west (Negredo et al., 2022; Manjón-Cabeza Córdoba & Ballmer, 2022). While this scenario is plausible and compatible with Civiero’s model, further study with expanded coverage of the study area using RFs is necessary to thoroughly test it.

By utilizing the Clapeyron slope of the olivine and ringwoodite PT, it becomes possible to estimate the total temperature variations across the MTZ beneath both archipelagos. If we substitute $\gamma_{660} = -2.0$ MPa/K, $\gamma_{410} = +4.00$ MPa/K and a reference MTZ thickness of 242 km from Lawrence and Shearer (2006) global RFs study in Eq. 4, the average MTZ thickness beneath the Canary archipelago (216 ± 2 km) translates to a temperature difference of $+144 \pm 11$ K. Similarly, the average MTZ thickness beneath the Madeira archipelago (237 ± 2 km) translates to a temperature difference of $+33 \pm 11$ K. These estimates provide insights into the thermal structure of the mantle anomalies beneath these volcanic regions. Excess temperatures within the mantle beneath these volcanic islands were independently confirmed using the chemical composition of the olivines, the liquidus phase of the alkaline magmas erupting on them (Putirka, 2008).

5.4 Evidences of thermochemical plume beneath the Canaries

The detection of *PXs* (also named *P300s* throughout the article) serves as compelling evidence for the existence of chemical heterogeneities within the plume material.

5.4.1 The X discontinuity

The X discontinuity has been observed in a variety of tectonic environments: subduction zones (Zhang & Lay, 1993; Schmerr, 2015), stable continents (Wajeman, 1988; Pugh et al., 2023), several hotspots (Courtier et al., 2007; Bagley & Revenaugh, 2008; Schmerr, 2015; Kemp et al., 2019; Pugh et al., 2021, 2023), and ridges (Schmerr, 2015). However, it seems not to be omnipresent throughout the planet (e.g., Williams & Revenaugh, 2005; Schmerr et al., 2013). This suggests that such discontinuity is probably linked to some form of mantle heterogeneity(ies) promoting a specific PT. These observations over a broad range of possible mantle temperatures have led to several explanations for the X (summarized in Table S3). Out of the different mechanisms that have been proposed to explain the X discontinuity, the silica phase transition from coesite to stishovite has been suggested as the most plausible explanation for the X in hot mantle upwellings, such as the Canary archipelago, where it was previously observed (Pugh et al., 2021). The presence of this discontinuity implies the presence of polymorphic silica-rich phases beneath the study region at these depths. Within a plume setting, this material might correspond to recycled eclogite, more silica-rich than the dominant peridotite, aligning with thermochemical plume models (Kemp et al., 2019; Pugh et al., 2021, 2023).

The presence of eclogite beneath hotspots may be explained by bidirectional mass transfer in the dynamic Earth’s interior, in agreement with a general model first proposed

577 by Hofmann and White (1982). The basaltic oceanic crust is recycled in the mantle through
 578 subduction, leading to the production of eclogitic rocks, denser than the dominant ul-
 579 trabasic compositions (peridotites in the upper mantle) (Niu, 2018). This process con-
 580 tributes to the formation of chemical heterogeneities that gradually accumulate near the
 581 base of the lower mantle, forming what are known as slab graveyards (e.g., van der Meer
 582 et al., 2018; Jones et al., 2021). These heterogeneities partially explain the origin of LLSVPs
 583 (Koppers et al., 2021), which are located beneath Africa and the Pacific (e.g., French &
 584 Romanowicz, 2015). LLSVPs are believed to serve as nurseries for major deep-mantle-
 585 sourced hotspots like the Canary hotspot (Koppers et al., 2021). These upwellings, rooted
 586 in LLSVPs, transport recycled oceanic crust, including eclogite-type materials, to up-
 587 per levels of the mantle (Hofmann & White, 1982; Tackley, 2000; Koppers et al., 2021).
 588 Owing to uranium enrichment of oceanic crust during sea-water alteration and lead de-
 589 pletion during subduction-induced dehydration, high $^{206}\text{Pb}/^{204}\text{Pb}$ is considered the best
 590 geochemical proxy for the presence in the mantle of ancient recycled oceanic crust, which
 591 is considered the cause for the HIMU mantle component (e.g., White, 2015). Here, the
 592 term HIMU refers to a mantle component characterized by a secular evolution under "High
 593 μ ", where $\mu = \text{U}/\text{Pb}$; it is a typical geochemical signature found in some volcanic rocks,
 594 particularly those associated with hotspots and oceanic island basalts (OIBs). Lavas from
 595 both Canary (Gurenko et al., 2006, 2009; Day et al., 2010) and Madeira (e.g., Mata et
 596 al., 1998; Geldmacher & Hoernle, 2000; Gurenko et al., 2013) show evidence for the con-
 597 tribution of the HIMU mantle component, translated in moderately high $^{206}\text{Pb}/^{204}\text{Pb}$
 598 (up to 20.270 and up to 19.989, respectively). These isotopic signatures independently
 599 support the geophysical evidence for the presence of eclogites in the mantle upwellings
 600 associated with those volcanic provinces. Recent numerical modelling indicates that man-
 601 tle plumes can entrain about 20% basalt component as recycled eclogite, which leads to
 602 the formation of an eclogitic reservoir at depths of around 400 to 300 km (Ballmer et al.,
 603 2013; Dannberg & Sobolev, 2015). Since an eclogite proportion larger than 40% is re-
 604 quired to seismically observe the X discontinuity (Schmerr, 2015; Kemp et al., 2019; Pugh
 605 et al., 2021), it has been suggested that with time the accumulation of eclogite above the
 606 MTZ would increase to the levels required to detect the *PXs* phase (Pugh et al., 2021).

607 The absence of a consistent *PXs* phase beneath Madeira suggests that, if a basalt
 608 reservoir is present, it likely contains less than 40% basalt. Conversely, localised detec-
 609 tions of the *PXs* phase beneath Madeira and the Canaries can be interpreted as indi-
 610 cations of localised accumulations of basalt.

611 Furthermore, it is plausible to hypothesise that the accumulation of the basalt reser-
 612 voir beneath the Canary Islands is facilitated by the long-lasting and continuous hotspot
 613 feeding up to the present day. In contrast, if Madeira is in a declining phase, the accu-
 614 mulation of this reservoir may have been comparatively less efficient and/or may have
 615 already diminished after the downward retreat of the denser eclogite material, after the
 616 decrease of the plume positive buoyancy.

617 **5.4.2 Compositional constraints from amplitude analysis**

618 A mechanical mixture (MM) of basalt (MORB) and harzburgite, with basalt in-
 619 creasing with depth, accurately replicates the seismic data for realistic thermal struc-
 620 tures of the upper mantle (Cammarano et al., 2009). First principle calculations indi-
 621 cate that the depth variations of the MTZ discontinuities are primarily influenced by tem-
 622 perature, whereas the magnitude of the corresponding velocity jumps is mainly affected
 623 by composition (e.g., Xu et al., 2008). Applying a simplified theoretical analysis to con-
 624 strain the basalt proportion above the MTZ, we utilize the velocity contrast obtained
 625 in the amplitude analysis of the detected phases and the velocity contrast in a MM model
 626 of the mantle.

627 Theoretical velocity contrasts for the co→st, ol→wa and ri→br+mw phases are com-
 628 puted from the velocity models of Xu et al. (2008) for a potential temperature of 1800
 629 K and basalt proportions ranging from 0% to 80%. Notably, the 410 discontinuity in these
 630 models aligns with the estimated depth beneath the Canaries, where a consistent *PXs*
 631 phase is detected. The predicted shear wave velocity jumps at depths of 300 km, 410 km,
 632 and 660 km, corresponding to the mentioned PT, are depicted in Figure 8 and summa-
 633 rized in the first four columns of Table 2. The analysis reveals that as the proportion
 634 of basalt increases, the velocity jumps for the 410 and 660 decrease, whereas the trend
 635 is opposite for the X discontinuity.

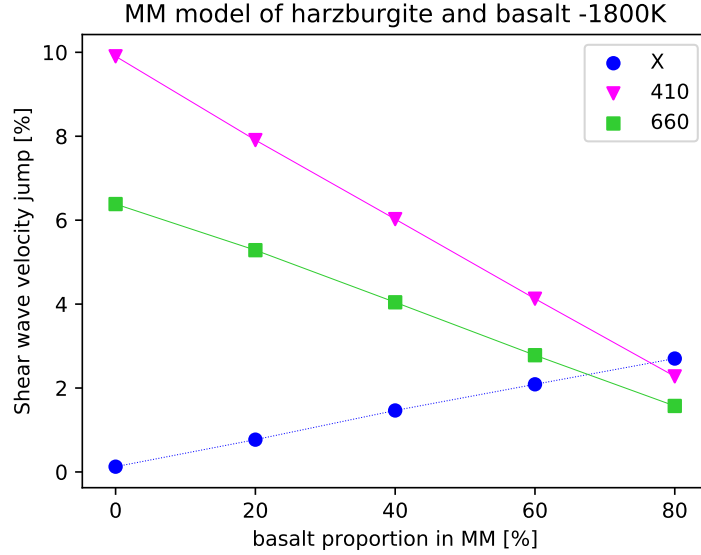


Figure 8. Predicted shear wave velocity jumps (in %) at depths of 300 km, 410 km, and 660 km, observed in a mechanical mixture (MM) of harzburgite and basalt with varying basalt proportions (f_b), obtained using the formula $V_{Sjump} = (v_2 - v_1)/2(v_1 + v_2)$, where v_1 and v_2 represent the velocities of the upper and lower layers, respectively.

basalt [%] f_b	v_s jump [%]			relative v_s jump	
	300	410	660	410/300	410/660
0	0.18	9.94	7.37	-	1.34
20	0.82	7.97	5.96	9.72	1.34
40	1.46	6.04	4.55	4.14	1.33
60	2.08	4.15	3.11	1.99	1.33
80	2.70	2.25	1.65	0.83	1.35

Table 2. Predicted shear wave velocity jumps at depths of 300 km, 410 km, and 660 km, observed in a mechanical mixture of harzburgite and basalt with varying proportions of basalt, f_b and a potential temperature of 1800 K. The last two columns display the relative velocity jumps between 410 and 300, and 410 and 660 as the proportion of basalt increases.

636 Our estimated velocity jumps (column four in Table 1) are obtained from the am-
 637 plitude analysis of detected converted phases. These phases can be difficult to detect on

individual RFs as arrivals are often relatively weak and close to the noise level. Occasionally, some phases show anomalously large amplitudes, in which case they can be identified individually. Generally, these signals are most reliably detected when a large number of RFs from small CCP areas are stacked but even then converted phases can be weak, thus making it challenging to robustly identify them. For example, for *P300s*, we only obtained 18 robust detections out of 34 good-quality CCP stacks. Moreover, the amplitude of converted phases in stacked RFs exhibits variability due to factors such as noise, focusing, and defocusing by small-scale topography variations. Consequently, constraints on absolute velocity jumps based on these amplitudes may not be accurate. Therefore, rather than interpreting the absolute values of velocity jumps, we focus on the relative values of the estimated velocity jumps (last two columns of Table 1). The corresponding theoretical values (relative velocity jumps w.r.t the 410) for varying proportions of basalt are displayed in the last two columns of Table 2. This theoretical analysis reveals that the relative velocity jump between the 410 and 660 remains relatively constant for varying fractions of basalt. However, the relative velocity jump between the 410 and X decreases as the proportion of basalt increases. In other words, the strength of the X discontinuity becomes more prominent for higher values of f_b , while the opposite trend is observed for the 410 and 660 discontinuities.

Our estimations for the relative velocity jumps between the 410 and X are 0.96 and 1.6 (Table 1), for the Canary and Madeira archipelagos, respectively. These values correspond to a proportion of basalt between 60% and 80% (Table 2). Based on the reliability of the X discontinuity in the Canaries dataset, we conclude that the accumulation of basalt is more significant there. For Madeira, the accumulation of basalt appears to be very localized.

6 Conclusions

Using P RFs, we conduct a systematic regional study to map out mantle seismic discontinuities beneath the Madeira and Canary archipelagos. We identify converted phases beneath both archipelagos for transition zone discontinuities, namely the 410 and 660. In the Canary Islands, the 410 is deeper (428 ± 4 km) and the 660 is shallower (647 ± 2 km). The MTZ is thinner (216 ± 2 km) compared to the global average suggesting the presence of a hot mantle upwelling characterised by excess temperatures that we estimate of $+144 \pm 11$ K with respect to the surrounding mantle. Furthermore, the dominant minerals influencing the topography of the 410 and 660 are, respectively, olivine and its polymorph ringwoodite. The discontinuity sharpness analysis provides additional support to this conclusion, as it reveals clear and well-defined 660 discontinuity features, which is in contrast to a broad 660 that would arise due to garnet being the dominant mineral. Beneath Madeira, the 660 discontinuity is close to the reference value and the 410 discontinuity is found at greater depths (421 ± 3 km). Here the MTZ is cooler than below the Canaries, with estimated excess temperatures of only $+33 \pm 11$ K with respect to the surrounding mantle. Furthermore, beneath the Canaries, we have reliable detections of the X discontinuity, attributed to the coesite-to-stishovite PT in regions of the upper mantle enriched in eclogite (as expected for thermochemical plumes). The X discontinuity is in the range of 251-316 km depth in a broad area beneath the Canaries, but it is observed at only one isolated location beneath Madeira at 313 km. We estimate that the basalt proportion in the plume, between 300-400 km, is 60-80%, with accumulation being more significant in the Canaries than in Madeira. The MTZ thickness, the presence of the X discontinuity, and the high basalt fraction provide compelling evidence for a deep-seated thermochemical plume beneath the study area, which feeds an active upwelling that presently crosses the MTZ beneath the Canaries. Beneath Madeira, it appears that only the upper portion of the MTZ is slightly affected. This suggests that the upwelling in this area might be less vigorous or currently disconnected from its deeper

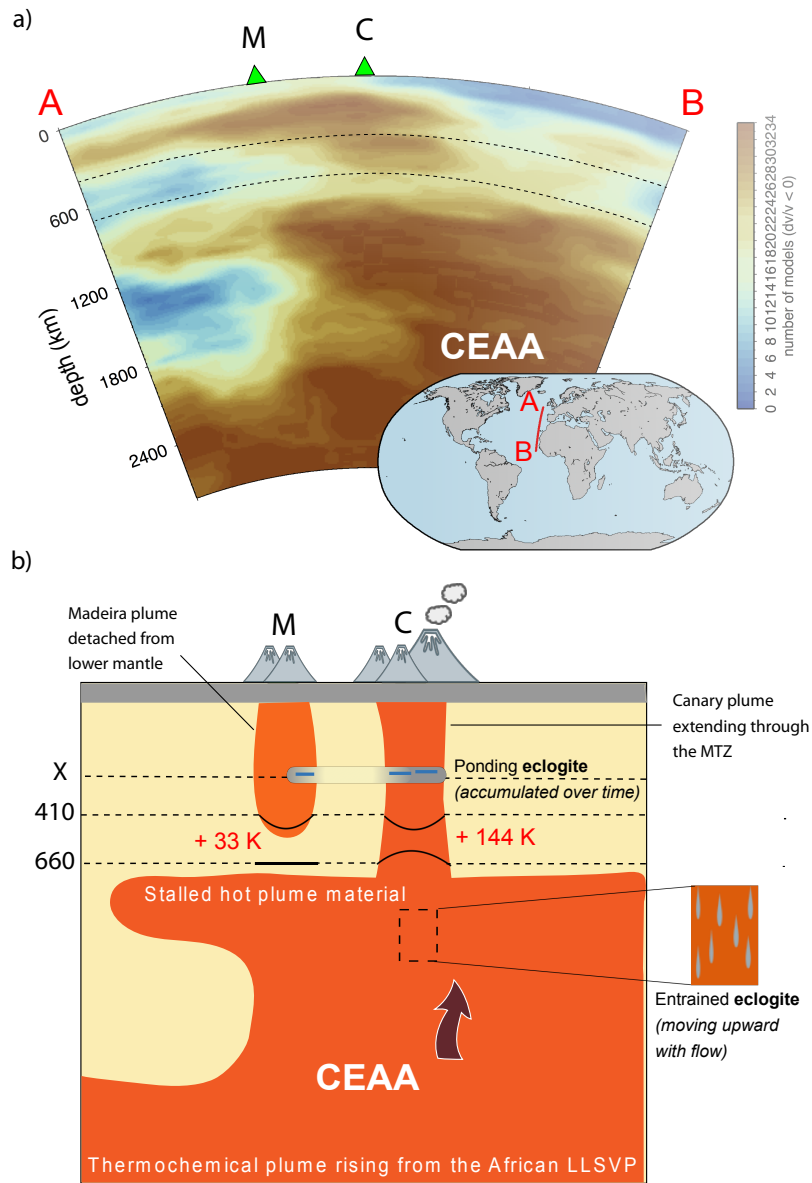


Figure 9. a) Vote cross-section created with the SubMachine tool (<http://www.earth.ox.ac.uk/smachine/>) using 34 P- and S-wave tomographic models and illustrating the most robust long-wavelength low-velocity anomalies in the mantle beneath Canaries (C) and Madeira (M). b) Cartoon illustrating the Canary Plume's extension through the upper mantle and the detached Madeira upwelling, incorporating constraints from our analysis (X discontinuity, eclogite above the MTZ, topography of MTZ discontinuities and temperature of MTZ).

689 source. This interpretation is in line with tomographic images. We have summarized our
 690 findings in the conceptual model presented in Figure 9.

691 Open Research Section

692 Data from IPMA permanent stations (PM) are available from IPMA at [http://](http://ceida.ipma.pt)
 693 ceida.ipma.pt. Data from DOCTAR experiment (Y7) are available on request from
 694 the GFZ at <https://dataservices.gfz-potsdam.de/portal/>. Data from the Global
 695 Seismograph Network (IU) are available from the IRIS Data Management Center (IRIS-
 696 DMC): <http://service.iris.edu/fdsnws/dataselect/1/>. Data from the Spanish Dig-
 697 ital Seismic Network (ES) are available on request from the Institut Cartogràfic i Geològic
 698 de Catalunya (ICGC): <http://ws.icgc.cat/fdsnws/dataselect/1/>.
 699 DOI information or FDSN network information, where available, are:
 700 IU: <https://doi.org/10.7914/SN/IU>
 701 ES: <https://10.7914/SN/ES>
 702 Y7: https://www.fdsn.org/networks/detail/Y7_2011/

703 Acknowledgments

704 We thank the associate editor and two anonymous reviewers for thoughtful comments
 705 and suggestions that helped improving the paper. This work is a contribution to projects
 706 SIGHT (Ref. PTDC/CTA-GEF/30264/2017) and GEMMA (PTDC/CTA-GEO/2083/2021).
 707 This work was also supported by the Portuguese Fundação para a Ciência e a Tecnolo-
 708 gia (FCT) I.P./MCTES through national funds (PIDDAC) – UIDB/50019/2020. LB would
 709 like to express sincere gratitude to the University of La Serena’s Research Incentive Pro-
 710 gram for Academics (PIA) for their generous support.

711 References

- 712 Aki, K., & Richards, P. (2002). *Quantitative Seismology*. University Science Books.
- 713 Allègre, C. J., & Turcotte, D. L. (1986). Implications of a two-component marble-
 714 cake mantle. , *323*(6084), 123-127. doi: 10.1038/323123a0
- 715 Ammon, C. J. (1991). The isolation of receiver effects from teleseismic P waveforms.
 716 *Bull. Seism. Soc. Am.*, *81*(6), 2504-2510. doi: 10.1785/BSSA0810062504
- 717 Bagley, B., & Revenaugh, J. (2008). Upper mantle seismic shear discontinuities of
 718 the Pacific. *Journal of Geophysical Research: Solid Earth*, *113*(B12). doi: 10
 719 .1029/2008JB005692
- 720 Ballmer, M. D., Ito, G., Wolfe, C. J., & Solomon, S. C. (2013). Double layering of a
 721 thermochemical plume in the upper mantle beneath Hawaii. *Earth and Planetary
 722 Science Letters*, *376*, 155–164. doi: 10.1016/j.epsl.2013.06.022
- 723 Bina, C. R., & Helffrich, G. (1994). Phase transition Clapeyron slopes and tran-
 724 sition zone seismic discontinuity topography. *Journal of Geophysical Research*,
 725 *99*(B8), 15853-15860. doi: 10.1029/94JB00462
- 726 Bonatto, L., Piromallo, C., & Cottaar, S. (2020). The Transition Zone Be-
 727 neath West Argentina-Central Chile Using P-to-S Converted Waves. *Jour-
 728 nal of Geophysical Research: Solid Earth*, *125*(8), e2020JB019446. doi:
 729 10.1029/2020JB019446
- 730 Bonatto, L., Schimmel, M., Gallart, J., & Morales, J. (2015). The upper-mantle
 731 transition zone beneath the Ibero-Maghrebian region as seen by teleseismic
 732 *Pds* phases . *Tectonophysics*, *663*, 212 - 224. (Special issue on Iberia geo-
 733 dynamics: An integrative approach from the Topo-Iberia framework) doi:
 734 10.1016/j.tecto.2015.02.002
- 735 Bostock, M. G. (1999). Seismic waves converted from velocity gradient anomalies
 736 in the Earth’s upper mantle. *Geophys. J. Int.*, *138*(3), 747-756. doi: 10.1046/
 737 j.1365-246X.1999.00902.x

- 738 Cammarano, F., Romanowicz, B., Stixrude, L., Lithgow-Bertelloni, C., & Xu, W.
739 (2009). Inferring the thermochemical structure of the upper mantle from
740 seismic data. *Geophysical Journal International*, *179*(2), 1169-1185. doi:
741 10.1111/j.1365-246X.2009.04338.x
- 742 Carracedo, J. C., & Troll, V. R. (2021). North-East Atlantic Islands: The Macarone-
743 sian Archipelagos. In D. Alderton & S. A. Elias (Eds.), *Encyclopedia of geol-
744 ogy (second edition)* (Second Edition ed., p. 674-699). Oxford: Academic Press.
745 doi: 10.1016/B978-0-08-102908-4.00027-8
- 746 Civiero, C., Armitage, J. J., Goes, S., & Hammond, J. O. S. (2019). The Seis-
747 mic Signature of Upper-Mantle Plumes: Application to the Northern East
748 African Rift. *Geochemistry, Geophysics, Geosystems*, *20*(12), 6106-6122. doi:
749 10.1029/2019GC008636
- 750 Civiero, C., Custódio, S., Neres, M., Schlaphorst, D., Mata, J., & Silveira, G. (2021).
751 The Role of the Seismically Slow Central-East Atlantic Anomaly in the Gen-
752 esis of the Canary and Madeira Volcanic Provinces. *Geophysical Research
753 Letters*, *48*(13), e92874. doi: 10.1029/2021GL092874
- 754 Civiero, C., Custódio, S., Rawlinson, N., Strak, V., Silveira, G., Arroucau, P.,
755 & Corela, C. (2019). Thermal Nature of Mantle Upwellings Below the
756 Ibero-Western Maghreb Region Inferred From Teleseismic Tomography.
757 *Journal of Geophysical Research: Solid Earth*, *124*(2), 1781-1801. doi:
758 10.1029/2018JB016531
- 759 Civiero, C., Strak, V., Custódio, S., Silveira, G., Rawlinson, N., Arroucau, P., &
760 Corela, C. (2018). A common deep source for upper-mantle upwellings
761 below the Ibero-western Maghreb region from teleseismic P-wave travel-
762 time tomography. *Earth and Planetary Science Letters*, *499*, 157-172. doi:
763 10.1016/j.epsl.2018.07.024
- 764 Collier, J. D., & Helffrich, G. R. (2001). The thermal influence of the subducting
765 slab beneath South America from 410 and 660 km discontinuity observations.
766 *Geophys. J. Int.*, *147*(2), 319-329. doi: 10.1046/j.1365-246X.2001.00532.x
- 767 Courtier, A. M., Bagley, B., & Revenaugh, J. (2007). Whole mantle discontinuity
768 structure beneath Hawaii. *Geophysical Research Letters*, *34*(17). doi: 10.1029/
769 2007GL031006
- 770 Crotwell, H. P., Owens, T. J., & Ritsema, J. (1999). The TauP Toolkit: Flexible
771 seismic travel-time and ray-path utilities. *Seismological Research Letters*, *70*,
772 154-160. doi: 10.1785/gssrl.70.2.154
- 773 Dannberg, J., & Sobolev, S. V. (2015). Low-buoyancy thermochemical plumes re-
774 solve controversy of classical mantle plume concept. *Nature communications*,
775 *6*(1), 1-9. doi: 10.1038/ncomms7960
- 776 Day, J. M. D., Pearson, D. G., Macpherson, C. G., Lowry, D., & Carracedo, J. C.
777 (2010). Evidence for distinct proportions of subducted oceanic crust and
778 lithosphere in HIMU-type mantle beneath El Hierro and La Palma, Ca-
779 nary Islands. *Geochimica et Cosmochimica Acta*, *74*(22), 6565-6589. doi:
780 10.1016/j.gca.2010.08.021
- 781 Deuss, A. (2007). Seismic observations of transition-zone discontinuities beneath
782 hotspot locations. *Special Paper 430: Plates, Plumes and Planetary Processes*,
783 121-136. doi: 10.1130/2007.2430(07)
- 784 Deuss, A. (2009). Global Observations of Mantle Discontinuities Using SS and PP
785 Precursors. *Surveys in Geophysics*, *30*(4-5), 301-326. doi: 10.1007/s10712-009
786 -9078-y
- 787 Deuss, A., Redfern, S. A. T., Chambers, K., & Woodhouse, J. H. (2006). The
788 Nature of the 660-Kilometer Discontinuity in Earth's Mantle from Global
789 Seismic Observations of PP Precursors. *Science*, *311*(5758), 198-201. doi:
790 10.1126/science.1120020
- 791 Dziewonski, A. M., & Anderson, D. L. (1981). Preliminary reference Earth model.
792 *Physics of the Earth and Planetary Interiors*, *25*(4), 297 - 356. doi: 10.1016/

- 793 0031-9201(81)90046-7
- 794 French, S., & Romanowicz, B. (2015). Broad plumes rooted at the base of
795 the Earth's mantle beneath major hotspots. *Nature*, *525*, 95-99. doi:
796 10.1038/nature14876
- 797 Geldmacher, J., & Hoernle, K. (2000). The 72 Ma geochemical evolution of the
798 Madeira hotspot (eastern North Atlantic): recycling of Paleozoic (500 Ma)
799 oceanic lithosphere. *Earth and Planetary Science Letters*, *183*(1), 73-92. doi:
800 10.1016/S0012-821X(00)00266-1
- 801 Geldmacher, J., Hoernle, K., Bogaard, P., Duggen, S., & Werner, R. (2005).
802 New ⁴⁰Ar/³⁹Ar age and geochemical data from seamounts in the Ca-
803 nary and Madeira volcanic provinces: Support for the mantle plume hy-
804 pothesis. *Earth and Planetary Science Letters*, *237*(1), 85-101. doi:
805 10.1016/j.epsl.2005.04.037
- 806 Geldmacher, J., Hoernle, K., van den Bogaard, P., Zankl, G., & Garbe-Schönberg,
807 D. (2001). Earlier history of the 70-Ma-old Canary hotspot based on the
808 temporal and geochemical evolution of the Selvagen Archipelago and neigh-
809 boring seamounts in the eastern North Atlantic. *Journal of Volcanology and*
810 *Geothermal Research*, *111*(1), 55-87. doi: 10.1016/S0377-0273(01)00220-7
- 811 Gu, Y. J., An, Y., Sacchi, M., Schultz, R., & Ritsema, J. (2009). Mantle reflectivity
812 structure beneath oceanic hotspots. *Geophysical Journal International*, *178*(3),
813 1456-1472. doi: 10.1111/j.1365-246X.2009.04242.x
- 814 Gurenko, A. A., Geldmacher, J., Hoernle, K. A., & Sobolev, A. V. (2013). A
815 composite, isotopically-depleted peridotite and enriched pyroxenite source
816 for Madeira magmas: Insights from olivine. *Lithos*, *170*, 224-238. doi:
817 10.1016/j.lithos.2013.03.002
- 818 Gurenko, A. A., Hoernle, K. A., Hauff, F., Schmincke, H. U., Han, D., Miura, Y. N.,
819 & Kaneoka, I. (2006). Major, trace element and Nd-Sr-Pb-O-He-Ar isotope
820 signatures of shield stage lavas from the central and western Canary Islands:
821 Insights into mantle and crustal processes. *Chemical Geology*, *233*(1-2), 75-112.
822 doi: 10.1016/j.chemgeo.2006.02.016
- 823 Gurenko, A. A., Sobolev, A. V., Hoernle, K. A., Hauff, F., & Schmincke, H.-U.
824 (2009). Enriched, HIMU-type peridotite and depleted recycled pyroxenite in
825 the Canary plume: A mixed-up mantle. *Earth and Planetary Science Letters*,
826 *277*(3-4), 514-524. doi: 10.1016/j.epsl.2008.11.013
- 827 Helffrich, G. (2000). Topography of the transition zone seismic discontinuities. *Re-*
828 *views of Geophysics*, *38*(1), 141-158. doi: 10.1029/1999RG000060
- 829 Helffrich, G., & Bina, C. R. (1994). Frequency dependence of the visibility and
830 depths of mantle seismic discontinuities. *Geophysical Research Letters*, *21*(24),
831 2613-2616. doi: <https://doi.org/10.1029/94GL02341>
- 832 Helffrich, G. R., & Wood, B. J. (2001). The Earth's mantle. , *412*(6846), 501-507.
833 doi: <https://doi.org/10.1038/35087500>
- 834 Hirose, K. (2002). Phase transitions in pyrolitic mantle around 670-km depth: Im-
835 plications for upwelling of plumes from the lower mantle. *Journal of Geophysi-*
836 *cal Research: Solid Earth*, *107*(B4), ECV 3-1-ECV 3-13. doi: [https://doi.org/](https://doi.org/10.1029/2001JB000597)
837 [10.1029/2001JB000597](https://doi.org/10.1029/2001JB000597)
- 838 Hofmann, A. W., & White, W. M. (1982). Mantle plumes from ancient oceanic
839 crust. *Earth and Planetary Science Letters*, *57*(2), 421-436. doi: 10.1016/0012-
840 -821X(82)90161-3
- 841 Houser, C., Masters, G., Flanagan, M., & Shearer, P. (2008). Determination and
842 analysis of long-wavelength transition zone structure using SS precursors. *Geo-*
843 *physical Journal International*, *174*(1), 178-194. doi: 10.1111/j.1365-246X.2008
844 .03719.x
- 845 Instituto Português do Mar e da Atmosfera, I.P. (2006). *Portuguese National*
846 *Seismic Network*. International Federation of Digital Seismograph Net-
847 works. Retrieved from <https://www.fdsn.org/networks/detail/PM/> doi:

- 848 10.7914/SN/PM
- 849 Jenkins, J., Deuss, A., & Cottaar, S. (2017). Converted phases from sharp 1000 km
850 depth mid-mantle heterogeneity beneath Western Europe. *Earth and Planetary
851 Science Letters*, 459, 196-207. doi: 10.1016/j.epsl.2016.11.031
- 852 Jones, T. D., Sime, N., & van Keken, P. E. (2021). Burying Earth's Primitive
853 Mantle in the Slab Graveyard. *Geochemistry, Geophysics, Geosystems*, 22(3),
854 e2020GC009396. doi: 10.1029/2020GC009396
- 855 Juliá, J. (2007). Constraining velocity and density contrasts across the
856 crust—mantle boundary with receiver function amplitudes. *Geophys. J. Int.*,
857 171(1), 286-301. doi: 10.1111/j.1365-2966.2007.03502.x
- 858 Kemp, M., Jenkins, J., MacLennan, J., & Cottaar, S. (2019). X-discontinuity
859 and transition zone structure beneath Hawaii suggests a heterogeneous
860 plume. *Earth and Planetary Science Letters*, 527, 115781. doi: 10.1016/
861 j.epsl.2019.115781
- 862 Koppers, A. A. P., Becker, T. W., Jackson, M. G., Konrad, K., Müller, R. D.,
863 Romanowicz, B., ... Whittaker, J. M. (2021). Mantle plumes and
864 their role in Earth processes. *Nat Rev Earth Environ*, 2, 382-401. doi:
865 10.1038/s43017-021-00168-6
- 866 Langston, C. A. (1979). Structure under Mount Rainier, Washington, inferred from
867 teleseismic body waves. *J. Geophys. Res.*, 84(B9), 4749-4762. doi: 10.1029/
868 JB084iB09p04749
- 869 Lawrence, J. F., & Shearer, P. M. (2006). A global study of transition zone thick-
870 ness using receiver functions. *Journal of Geophysical Research: Solid Earth*,
871 111(B6). doi: 10.1029/2005JB003973
- 872 Lawrence, J. F., & Shearer, P. M. (2008). Imaging mantle transition zone thickness
873 with SdS-SS finite-frequency sensitivity kernels. *Geophysical Journal Interna-
874 tional*, 174(1), 143-158. doi: 10.1111/j.1365-246X.2007.03673.x
- 875 Li, C., van der Hilst, R. D., Engdahl, E. R., & Burdick, S. (2008). A new global
876 model for P wave speed variations in Earth's mantle. *Geochemistry, Geo-
877 physics, Geosystems*, 9(5). (Q05018) doi: 10.1029/2007GC001806
- 878 Li, X., Kind, R., & Yuan, X. (2003). Seismic study of upper mantle and transition
879 zone beneath hotspots. *Physics of the Earth and Planetary Interiors*, 136(1-2),
880 79-92. doi: 10.1016/S0031-9201(03)00021-9
- 881 Liu, H., Wang, W., Jia, X., Leng, W., Wu, Z., & Sun, D. (2018, August). The
882 combined effects of post-spinel and post-garnet phase transitions on man-
883 tle plume dynamics. *Earth and Planetary Science Letters*, 496, 80-88. doi:
884 10.1016/j.epsl.2018.05.031
- 885 Manjón-Cabeza Córdoba, A., & Ballmer, M. D. (2022). The role of edge-driven
886 convection in the generation of volcanism – Part 2: Interaction with mantle
887 plumes, applied to the Canary Islands. *Solid Earth*, 13(10), 1585-1605. doi:
888 10.5194/se-13-1585-2022
- 889 Martínez-Arevalo, C., Mancilla, F. d. L., Helffrich, G., & Garcia, A. (2013). Seismic
890 evidence of a regional sublithospheric low velocity layer beneath the Canary
891 Islands. *Tectonophysics*, 608, 586-599. doi: 10.1016/j.tecto.2013.08.021
- 892 Mata, J., Kerrich, R., MacRae, N. D., & Wu, T. W. (1998). Elemental and isotopic
893 (Sr, Nd, and Pb) characteristics of Madeira Island basalts: evidence for a com-
894 posite HIMU - EM I plume fertilizing lithosphere. *Canadian Journal of Earth
895 Sciences*, 35(9), 980-997. doi: 10.1139/e98-046
- 896 Matos, C., Silveira, G., Matias, L., Caldeira, R., Ribeiro, M. L., Dias, N. A., ...
897 Bento dos Santos, T. (2015). Upper crustal structure of madeira island re-
898 vealed from ambient noise tomography. *Journal of Volcanology and Geothermal
899 Research*, 298, 136-145. doi: 10.1016/j.jvolgeores.2015.03.017
- 900 Morgan, W. J. (1972). Plate Motions and Deep Mantle Convection. In *Studies
901 in Earth and Space Sciences*. Geological Society of America. doi: 10.1130/
902 MEM132-p7

- 903 Negredo, A. M., van Hunen, J., Rodríguez-González, J., & Fullea, J. (2022). On the
 904 origin of the Canary Islands: Insights from mantle convection modelling. *Earth
 905 and Planetary Science Letters*, *584*, 117506. doi: [https://doi.org/10.1016/j.epsl](https://doi.org/10.1016/j.epsl.2022.117506)
 906 [.2022.117506](https://doi.org/10.1016/j.epsl.2022.117506)
- 907 Niu, Y. (2018). Origin of the LLSVPs at the base of the mantle is a consequence of
 908 plate tectonics – A petrological and geochemical perspective. *Geoscience Fron-*
 909 *tiers*, *9*(5), 1265-1278. (SPECIAL ISSUE: Frontiers in geoscience: A tribute to
 910 Prof. Xuanxue Mo) doi: <https://doi.org/10.1016/j.gsf.2018.03.005>
- 911 Paulssen, H. (1988). Evidence for a Sharp 670-km Discontinuity as Inferred From P-
 912 to-s Converted Waves. *J. Geophys. Res.*, *93*(B9), 10489-10500. doi: [10.1029/
 913 JB093iB09p10489](https://doi.org/10.1029/JB093iB09p10489)
- 914 Phinney, R. (1964). Structure of the Earth's Crust from Spectral Behavior
 915 of Long-Period Body Waves. *J. Geophys. Res.*, *69*(14), 2997-3017. doi:
 916 [10.1029/JZ069i014p02997](https://doi.org/10.1029/JZ069i014p02997)
- 917 Pugh, S., Boyce, A., Bastow, I. D., Ebinger, C. J., & Cottaar, S. (2023). Multi-
 918 genetic Origin of the X-Discontinuity Below Continents: Insights From
 919 African Receiver Functions. *Geochemistry, Geophysics, Geosystems*, *24*(3),
 920 e2022GC010782. doi: [10.1029/2022GC010782](https://doi.org/10.1029/2022GC010782)
- 921 Pugh, S., Jenkins, J., Boyce, A., & Cottaar, S. (2021). Global receiver func-
 922 tion observations of the X-discontinuity reveal recycled basalt beneath
 923 hotspots. *Earth and Planetary Science Letters*, *561*, 116813. doi: [10.1016/
 924 j.epsl.2021.116813](https://doi.org/10.1016/j.epsl.2021.116813)
- 925 Putirka, K. (2008). Excess temperatures at ocean islands: Implications for mantle
 926 layering and convection. *Geology*, *36*(4), 283-286. doi: [10.1130/G24615A.1](https://doi.org/10.1130/G24615A.1)
- 927 Richards, P. (1972). Seismic waves reflected from velocity gradient anomalies within
 928 the Earth's upper mantle. *J. Geophys. Res.*, *38*, 517-527. doi: [10.1046/j.1365-
 929 -246x.1999.00902.x](https://doi.org/10.1046/j.1365-246x.1999.00902.x)
- 930 Ritsema, J., & Van Heijst, H. J. (2002). Constraints on the correlation of P-
 931 and S-wave velocity heterogeneity in the mantle from P, PP, PPP and
 932 PKPab travel times. *Geophys. J. Int.*, *149*(2), 482-489. doi: [10.1046/
 933 j.1365-246X.2002.01631.x](https://doi.org/10.1046/j.1365-246X.2002.01631.x)
- 934 Saki, M., Thomas, C., Nippres, S. E. J., & Lessing, S. (2015). Topography of upper
 935 mantle seismic discontinuities beneath the North Atlantic: The Azores, Canary
 936 and Cape Verde plumes. *Earth and Planetary Science Letters*, *409*, 193-202.
 937 doi: [10.1016/j.epsl.2014.10.052](https://doi.org/10.1016/j.epsl.2014.10.052)
- 938 Sandwell, D. T., Müller, R. D., Smith, W. H. F., Garcia, E., & Francis, R. (2014).
 939 New global marine gravity model from CryoSat-2 and Jason-1 reveals buried
 940 tectonic structure. *Science*, *346*(6205), 65-67. doi: [10.1126/science.1258213](https://doi.org/10.1126/science.1258213)
- 941 Schimmel, M., & Paulssen, H. (1997). Noise reduction and detection of weak, coher-
 942 ent signals through phase-weighted stacks. *Geophys. J. Int.*, *130*(2), 497-505.
 943 doi: [10.1111/j.1365-246X.1997.tb05664.x](https://doi.org/10.1111/j.1365-246X.1997.tb05664.x)
- 944 Schlaphorst, D., Silveira, G., Mata, J., Krüger, F., Dahm, T., & Ferreira, A. M. G.
 945 (2022). Heterogeneous seismic anisotropy beneath Madeira and Canary
 946 archipelagos revealed by local and teleseismic shear wave splitting. *Geophysical
 947 Journal International*, *233*(1), 510-528. doi: [10.1093/gji/ggac472](https://doi.org/10.1093/gji/ggac472)
- 948 Schmerr, N. (2015). Imaging mantle heterogeneity with upper mantle seismic dis-
 949 continuities. In A. Khan & F. Deschamps (Eds.), *The earth's heterogeneous
 950 mantle: A geophysical, geodynamical, and geochemical perspective* (pp. 79-104).
 951 Cham: Springer International Publishing. doi: [10.1007/978-3-319-15627-9_3](https://doi.org/10.1007/978-3-319-15627-9_3)
- 952 Schmerr, N. C., Kelly, B. M., & Thorne, M. S. (2013). Broadband array observa-
 953 tions of the 300 km seismic discontinuity. *Geophysical Research Letters*, *40*(5),
 954 841-846. doi: [10.1002/grl.50257](https://doi.org/10.1002/grl.50257)
- 955 Shearer, P. M., & Flanagan, M. P. (1999). Seismic Velocity and Density Jumps
 956 Across the 410- and 660-Kilometer Discontinuities. *Science*, *285*, 1545-1548.
 957 doi: [10.1126/science.285.5433.1545](https://doi.org/10.1126/science.285.5433.1545)

- 958 Tackley, P. J. (2000). Mantle Convection and Plate Tectonics: Toward an Integrated
 959 Physical and Chemical Theory. *Science*, *288*(5473), 2002-2007. doi: 10.1126/
 960 science.288.5473.2002
- 961 van der Meer, D. G., van Hinsbergen, D. J., & Spakman, W. (2018). Atlas of
 962 the underworld: Slab remnants in the mantle, their sinking history, and a
 963 new outlook on lower mantle viscosity. *Tectonophysics*, *723*, 309-448. doi:
 964 https://doi.org/10.1016/j.tecto.2017.10.004
- 965 van der Meijde, M., Marone, F., Giardini, D., & van der Lee, S. (2003). Seismic
 966 Evidence for Water Deep in Earth's Upper Mantle. *Science*, *300*(5625), 1556-
 967 1558. doi: 10.1126/science.1083636
- 968 Vidale, J. E., & Benz, H. M. (1992). Upper-mantle seismic discontinuities and the
 969 thermal structure of subduction zones. *Nature*, *356*(6371), 678-683. doi: 10
 970 .1038/356678a0
- 971 Vinnik, L. (1977). Detection of waves converted from P to SV in the mantle. *J.*
 972 *Phys. Earth Planet. Inter.*, *15*(1), 39-45. doi: 10.1016/0031-9201(77)90008-5
- 973 Wajeman, N. (1988). Detection of underside P reflections at mantle discontinuities
 974 by stacking broadband data. *Geophysical Research Letters*, *15*(7), 669-672. doi:
 975 10.1029/GL015i007p00669
- 976 Weidner, D. J., & Wang, Y. (1998). Chemical- and Clapeyron-induced buoyancy
 977 at the 660 km discontinuity. *Journal of Geophysical Research: Solid Earth*,
 978 *103*(B4), 7431-7441. doi: 10.1029/97JB03511
- 979 White, W. M. (2015). Isotopes, DUPAL, LLSVPs, and Anekantavada. *Chemical Ge-*
 980 *ology*, *419*, 10-28. doi: 10.1016/j.chemgeo.2015.09.026
- 981 Williams, Q., & Revenaugh, J. (2005). Ancient subduction, mantle eclogite, and the
 982 300 km seismic discontinuity. *Geology*, *33*(1), 1-4. doi: 10.1130/G20968.1
- 983 Xu, W., Lithgow-Bertelloni, C., Stixrude, L., & Ritsema, J. (2008). The effect of
 984 bulk composition and temperature on mantle seismic structure. *Earth and*
 985 *Planetary Science Letters*, *275*(1), 70 - 79. doi: 10.1016/j.epsl.2008.08.012
- 986 Yu, Y. G., Wentzcovitch, R. M., Vinograd, V. L., & Angel, R. J. (2011). Thermody-
 987 namic properties of MgSiO₃ majorite and phase transitions near 660 km depth
 988 in MgSiO₃ and Mg₂SiO₄: A first principles study. *Journal of Geophysical*
 989 *Research: Solid Earth*, *116*(B2), B02208. doi: 10.1029/2010JB007912
- 990 Zhang, Z., & Lay, T. (1993). Investigation of upper mantle discontinuities
 991 near Northwestern Pacific Subduction Zones using precursors to sSH.
 992 *Journal of Geophysical Research: Solid Earth*, *98*(B3), 4389-4405. doi:
 993 10.1029/92JB02050
- 994 Ziberna, L., Klemme, S., & Nimis, P. (2013). Garnet and spinel in fertile and de-
 995 pleted mantle: insights from thermodynamic modelling. *Contributions to Min-*
 996 *eralogy and Petrology*, *166*(2), 411-421. doi: 10.1007/s00410-013-0882-5

997 References from the Supporting Information

- 998 Akaogi, M., Takayama, H., Kojitani, H., Kawaji, H., & Atake, T. (2007). Low-
 999 temperature heat capacities, entropies and enthalpies of Mg₂SiO₄ polymorphs,
 1000 and α - β - γ and post-spinel phase relations at high pressure. *Phys Chem*
 1001 *Minerals*, *34*, 169-183, doi: 10.1007/s00269-006-0137-3
- 1002 Akaogi, M., & Akimoto, S.-I. (1980). High-pressure stability of a dense hydrous
 1003 magnesian silicate Mg₂₃Si₈O₄₂H₆ and some geophysical implications.
 1004 *Journal of Geophysical Research: Solid Earth*, *85* (B12), 6944-6948, doi:
 1005 10.1029/JB085iB12p06944
- 1006 Allen, R. V. (1978). Automatic earthquake recognition and timing from single
 1007 traces. *Bulletin of the Seismological Society of America*, *68* (5), 1521-1532,
 1008 doi:10.1785/BSSA0680051521
- 1009 Bonatto, L., Schimmel, M., Gallart, J., & Morales, J. (2015). The upper-mantle
 1010 transition zone beneath the Ibero-Maghrebian region as seen by teleseis-

- mic Pds phases [Special issue on Iberia geodynamics: An integrative approach from the Topo-Iberia framework]. *Tectonophysics*, 663, 212–224, doi:10.1016/j.tecto.2015.02.002
- Bonatto, L., Piromallo, C., & Cottaar, S. (2020). The Transition Zone Beneath West Argentina-Central Chile Using P-to-S Converted Waves. *Journal of Geophysical Research: Solid Earth*, 125 (8), e2020JB019446, doi:10.1029/2020JB019446
- Boyce, A., & Cottaar, S. (2021). Insights Into Deep Mantle Thermochemical Contributions to African Magmatism From Converted Seismic Phases. *Geochemistry, Geophysics, Geosystems*, 22 (3), Article e2020GC009478, e2020GC009478, doi:10.1029/2020GC009478
- Chen, T., Gwanmesia, G. D., Wang, X., Zou, Y., Liebermann, R. C., Michaut, C., & Li, B. (2015). Anomalous elastic properties of coesite at high pressure and implications for the upper mantle X-discontinuity. *Earth and Planetary Science Letters*, 412, 42–51, doi:10.1016/j.epsl.2014.12.025
- Clayton, R. W., & Wiggins, R. A. (1976). Source shape estimation and deconvolution of teleseismic body waves. *J. R. Astr. Soc.*, 47 (1), 151–177, doi:10.1111/j.1365-246X.1976.tb01267.x
- Dueker, K. G., & Sheehan, A. F. (1998). Mantle discontinuity structure beneath the Colorado Rocky Mountains and High Plains. *Journal of Geophysical Research: Solid Earth*, 103 (B4), 7153–7169, doi:10.1029/97JB03509
- Ganguly, J., & Frost, D. J. (2006). Stability of anhydrous phase B: Experimental studies and implications for phase relations in subducting slab and the X discontinuity in the mantle. *Journal of Geophysical Research: Solid Earth*, 111 (B6), doi:10.1029/2005JB003910
- Katsura, T., Yamada, H., Nishikawa, O., Song, M., Kubo, A., Shinmei, T., Yokoshi, S., Aizawa, Y., Yoshino, T., Walter, M. J., & Ito, E. (2004). Olivine-wadsleyite transition in the system (Mg,Fe)₂SiO₄. *J. Geophys. Res.*, 109, B02209, doi:10.1029/2003JB002438
- Kemp, M., Jenkins, J., MacLennan, J., & Cottaar, S. (2019). X-discontinuity and transition zone structure beneath Hawaii suggests a heterogeneous plume. *Earth and Planetary Science Letters*, 527, 115781, doi:10.1016/j.epsl.2019.115781
- Litasov, K. D., Ohtani, E., Sano, A., Suzuki, A., & Funakoshi, K. (2005). Wet subduction versus cold subduction. *Geophysical Research Letters*, 32 (13), doi:10.1029/2005GL022921
- Liu, J., Topor, L., Zhang, J., Navrotsky, A., & Liebermann, R. C. (1996). Calorimetric study of the coesite-stishovite transformation and calculation of the phase boundary. *Phys Chem Minerals*, 23, 11–16, doi:10.1007/BF00202988
- Pugh, S., Jenkins, J., Boyce, A., & Cottaar, S. (2021). Global receiver function observations of the X-discontinuity reveal recycled basalt beneath hotspots. *Earth and Planetary Science Letters*, 561, 116813, doi:10.1016/j.epsl.2021.116813
- Revenaugh, J., & Jordan, T. H. (1991). Mantle layering from ScS reverberations: 3. The upper mantle. *Journal of Geophysical Research: Solid Earth*, 96 (B12), 19781–19810, doi:10.1029/91JB01487
- Schmerr, N. (2015). Imaging mantle heterogeneity with upper mantle seismic discontinuities. In A. Khan F. Deschamps (Eds.), *The earth's heterogeneous mantle: A geophysical, geodynamical, and geochemical perspective* (pp. 79–104). Springer International Publishing, doi:10.1007/978-3-319-15627-9_3
- Williams, Q., & Revenaugh, J. (2005). Ancient subduction, mantle eclogite, and the 300 km seismic discontinuity. *Geology*, 33 (1), 1–4, doi:10.1130/G20968.1
- Woodland, A. B. (1998). The orthorhombic to high-P monoclinic phase transition in Mg-Fe Pyroxenes: Can it produce a seismic discontinuity? *Geophysical Research Letters*, 25 (8), 1241–1244, doi:10.1029/98GL00857
- Xu, W., Lithgow-Bertelloni, C., Stixrude, L., & Ritsema, J. (2008). The effect of bulk composition and temperature on mantle seismic structure. *Earth and*

- 1066 *Planetary Science Letters*, 275 (1), 70–79, doi:10.1016/j.epsl.2008.08.012
1067 Yu, Y., Wu, Z., & Wentzcovitch, R. (2008). Transformations in Mg_2SiO_4
1068 in Earth's transition zone. *Earth Planet. Sci. Lett.*, 273, 115–122,
1069 doi:10.1016/j.epsl.2008.06.023
1070 Yu, Y. G., Wentzcovitch, R. M., Vinograd, V. L., & Angel, R. J. (2011). Thermody-
1071 namic properties of MgSiO_3 majorite and phase transitions near 660 km depth
1072 in MgSiO_3 and Mg_2SiO_4 : A first principles study. *Journal of Geophysical*
1073 *Research (Solid Earth)*, 116 (B2), B02208, doi:10.1029/2010JB007912